

TECHNISCHE
UNIVERSITÄT
DRESDEN



Normalization Of Image Reconstruction In Positron Emission Tomography By Means Of A Homogeneous Phantom For Utilization In Lab Courses

Bachelor-Arbeit
zur Erlangung des Hochschulgrades
Bachelor of Science
im Bachelor-Studiengang Physik

vorgelegt von

Benas Sudzius
geboren am 18.05.1999 in Vilnius

Institut für Kern und Teilchen Physik
Fakultät Physik
Bereich Mathematik und Naturwissenschaften
Technische Universität Dresden
2021

Eingereicht am 24. Juni 2021

1. Gutachter: Prof. Dr. Arno Straessner
2. Gutachter: Prof. Dr. Kai Zuber

Abstract

English: Three dimensional positron emission tomography (PET) plays an important role in cancer soil studies by enabling detection and localization of tumor cells. This thesis investigates the ClearPET measuring system. Central matter of interest is the reconstruction process. There is to be examined how accurate the ClearPET can reconstruct known interrelations between source activities. The optimization of this process is accomplished by normalizing the reconstruction image by means of a homogeneous phantom. In case of this experimental setup the phantom is a cylinder with a homogeneous activity distribution.

Deutsch: Dreidimensionale Positronen-Emissions-Tomographie (PET) spielt eine wichtige Rolle in Krebsstudien, indem sie das Auftreten von Krebszellen nachweist. Diese Arbeit untersucht das ClearPET und insbesondere den Rekonstruktionsprozess. Es soll geprüft werden, ob bekannte Zusammenhänge bezüglich radioaktiver Quellen reproduziert werden können. Der Prozess soll durch eine Normalisierungsmessung mit einem homogenen Phantom verbessert werden. Hierbei handelt es sich um einen Zylinder mit gleichmäßiger Quellverteilung.

Contents

1	Introduction	5
2	Material and Methods	7
2.1	Measuring system	7
2.1.1	Measuring procedure	8
2.1.2	Cassettes	9
2.1.3	Homogeneous phantom	11
2.2	Physical background	12
2.2.1	Compton scattering	12
2.2.2	Attenuation coefficient	15
2.2.3	Types of radiation	15
2.2.4	Sodium-22 and related physical phenomena	16
2.3	Reconstruction process	19
2.3.1	Intensity and Beer's law	19
2.3.2	Radon transform and its inverse	19
2.3.3	OSMAPOSL algorithm	22
2.4	Fourier rebinning algorithm	23
3	Experimental results	25
3.1	Reconstruction routine	26
3.2	Back projection of point sources	26
3.2.1	Full width half maximum analysis of the strong point source	28
3.2.2	Investigation of the statistical error	29
3.2.3	Validation of the maxima approach	30
3.3	Comparison of activities and quantification of spatial reconstruction behavior .	31
3.4	Normalization measurement	32
3.5	Sinogram	34
3.6	Reconstruction with the OSMAPOSL algorithm	36
3.7	Implementation of attenuation correction and multiple iterations of the OSMAPOSL- algorithm	39
4	Summary	43

Bibliography	45
Appendix	49

1 Introduction

The ClearPET is a positron emission tomograph (PET) and was manufactured by raytest Isotopenmessgeräte GmbH. Positron emission refers to the production of a positron as a result of β^+ decay. This positron annihilates with an electron into two photons which move due to momentum conservation in antiparallel directions. Because of their antiparallel property, the two photons can be seen as a line of response (LOR) which can be detected by the cassettes of the measurement system. The goal of this thesis is to investigate the reconstruction step which would be the transformation from many LORs to the final activity image.

These activity images are a central point of interest in two major application areas. First of all positron emission tomographs are used in cancer diagnosis. The patients get injected with a solution including a radiotracer, namely fluorodeoxyglucose F 18, consisting of the β^+ emitter Fluorine-18 paired with a sugar molecule. The sugar molecule attaches to the tumorous cells, so if the Fluorine-18 is detected and accumulated in a suspected area one might identify tumorous cells. Fluorine-18 is chosen because of its half-life of about 109 minutes, so the patient does not suffer negative long term consequences. The resulting difficulty is a limited time span for measurements and the storage of an isotope with such a short half-life [1]. To allow for more systematic research the investigated β^+ emitter is Sodium-22 with a half-life of 2.6 years [2]. This allows to focus on measurements and prepare a lab course for conveying the basics of PET measurement systems. Another application for PET measuring systems is the investigation of fluids in rock layers. It is necessary for optimization of the extraction of raw materials, for example one can reproduce the flowing behavior of crude oil. Other considerable methods like magnetic resonance imaging (MRI) can not be applied because of the ferromagnetic properties of the investigated materials as carried out by Kulenkampff [3]. Thus, although the field of applications for PET measuring systems is very specific, PET systems separate themselves by being an unique solution for certain problems.

The foundation for working with the ClearPET at the IKTP for lab courses was elaborated by Lehr [4]. He accomplished the restoration of the ClearPET from a non functional state to a point where an activity image could be reconstructed. Furthermore he investigated the properties of the experimental setup, providing every further collaborator a reference regarding background knowledge and functionality of the system.

Another keystone in the experimental work could be accomplished with the help of Prof. Krause Rehberg. He provided the Sodium-22 solution which is the main part of the homogeneous phantom. Without this phantom the normalization measurement would not be possible which is the core part of this thesis.

Regarding background, requirements and opportunities the following aims for this thesis are defined:

- Improving the reconstruction of activities produced by β^+ emitters.
- Investigation of a normalization measurement by means of a homogeneous phantom and its impact on the reconstruction quality. This measurement improves the measured data by providing each measured point a reference value.
- Knowledge transfer: the majority of measurements and theoretical backgrounds should be of a manner that they can be reproduced by students in the lab courses.

2 Material and Methods

To understand the whole process, the background is discussed regarding three topics. First of all the measuring system is described. This will provide a basic and intuitive understanding of the detection methods before explaining the underlying physical processes. After that the core concepts of image reconstruction are explained. Especially the physical phenomena are of interest because their contemplation plays an important part in lab courses.

2.1 Measuring system

The ClearPET is depicted in figure 2.1. On the left side one can see the measuring system as a whole arrangement. The gantry can rotate and consists of the metallic frame which holds the cassettes. On the right side one can see the closeup of the field of view (FOV). On the top left and on the bottom right, one observes the cassettes which carry the detectors.

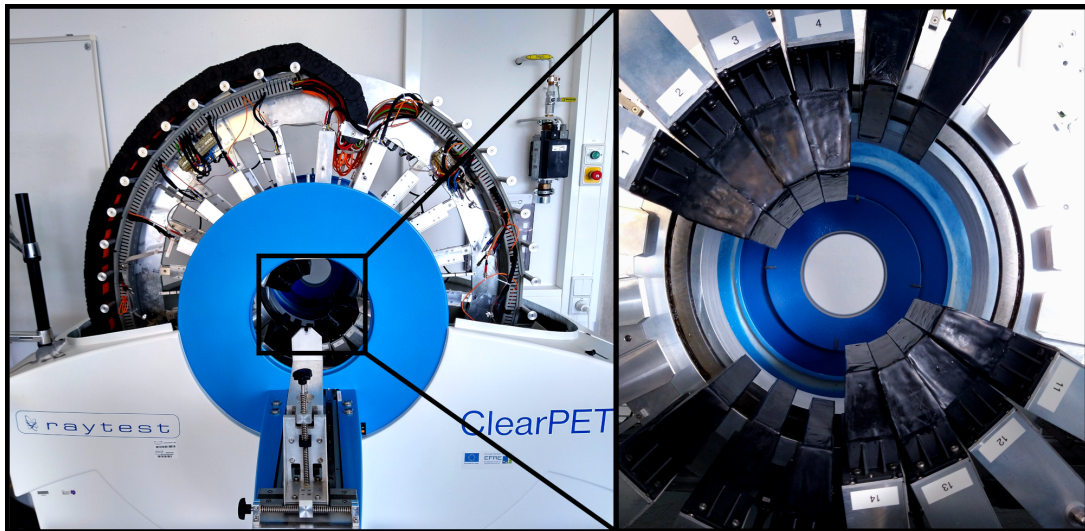


Figure 2.1: The ClearPET measuring system. On the right side one can see a closeup on the FOV.

One can clearly see that when the cassettes are rotated by the gantry a wider solid angle is covered. This compensates the fact that our particular measuring system only has eight cassettes instead of twenty possible. Although through the rotation the distribution of the detection events preserves cylindrical symmetry their amount decreases with decreasing number of cassettes. In medical practice this is an issue but regarding the fact that the investigated

isotope is Sodium-22 and not Fluorine-18 with a half-life of 2.6 years, it is possible to extend the measurement time if required with almost no upper limit. The rotation gives another important property which is the cylindrical symmetry. Therefore in this thesis the cylindrical coordinate system is utilized with the z-axis being the axial one. The x- and y-axis, forming the base of the cylinder, are referred to as transverse axes. Planes parallel to the basis are transverse planes and every plane perpendicular to the base plane is in our measurements a xz-, namely coronal plane. It is reasonable to only consider the coronal planes since due to the rotational symmetry every plane perpendicular to the transverse plane is theoretically equal.

2.1.1 Measuring procedure

The whole measuring process is schematically represented in the figure 2.2. The beginning point is the emission of a positron by the radioactive isotope. The electron and positron annihilate and emit two photons in opposite directions.

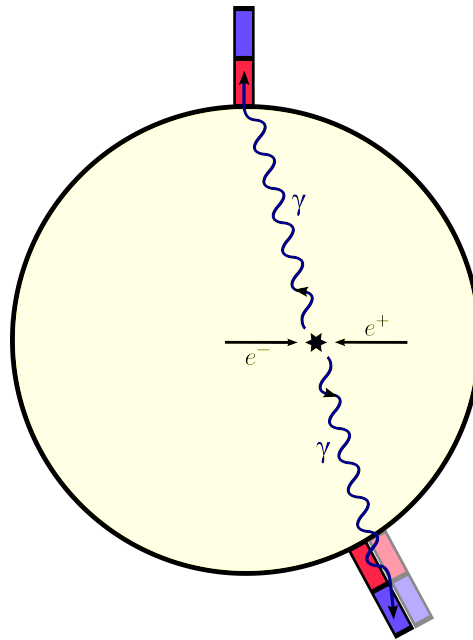


Figure 2.2: Schematic representation of the detection process. Including electron positron annihilation, the occurrence of two gamma rays producing a LOR and its detection utilizing the phoswich arrangement.

The photons are then detected by the detector bins which are represented by the combination of the red and blue rectangle. The circle however is referred to as ring. In the reconstruction process the detector works with 160 bins per ring, resulting from the rotation of the gantry. The scanner geometry is further discussed in section 2.1.2. At this point one focuses on another very unique feature of the ClearPET measuring system, namely the phoswich arrangement of the bins which is visualized by using two different colors for them.

2.1.2 Cassettes

To detect the photons, scintillation crystals are used. An incoming photon excites electrons of the crystal. The excited state recombines and emits a photon with a known wavelength and energy. The emitted photon is amplified in a photomultiplier tube (PMT). During the amplification process, the absorbed photon ejects electrons from the photocathode of the PMT. The ejected electrons are accelerated in an electric field before striking a dynode which leads to the emission of more low energy electrons. This process is repeated multiple times. In this way, the number of electrons gets remarkably enhanced such that the signal can be reliably processed and counted.

It is important to note that in figure 2.2 only one PMT for the red and blue bin exists. Therefore one needs a method to determine the bin where the interaction between incoming photon and crystal occurred. The crucial point is that one can determine a half-life for every excited state of the different scintillator materials. Because the deexcitation of states is described by Poisson statistics one fits the signal versus time behavior and obtains the half-life for the excited states leading to the corresponding crystal where the reaction occurred. Although fitting leads to the correct half-life it is computationally expensive. Therefore the pulse shape analysis considers in its computation only the difference of the last and the first value normed with the sum of all values. This difference is higher for the crystal with longer half-life when the time difference between first and last value is a constant. In this manner the spatial resolution can be improved. As seen in figure 2.2 there is the possibility that the γ ray crosses a bin without an interaction. Especially then it makes sense to distinguish the position of the interaction of photon with the detector. Regarding the ClearPET measuring system this is visualized using two different colors. The red part represents Lutetium-Yttrium Oxyorthosilicat (LYSO) which excited states have a half-life of 45 ns [5] and the blue part Lutetium-Yttrium Orthoaluminat (LuYAP) which excited states have a mixture of half-lives equal to 16 ns and 138 ns in ratio 2:3 [5]. The distinct half-lives allow to conclude the material where the photon reacted and therefore one knows its spatial origin. This behavior was investigated in depth by Lehr [4].

2.1.2 Cassettes

A further matter of interest are the cassettes which are shown in figure 2.3. One can observe that a cassette consists of four blocks each containing 8 times 8 bins.

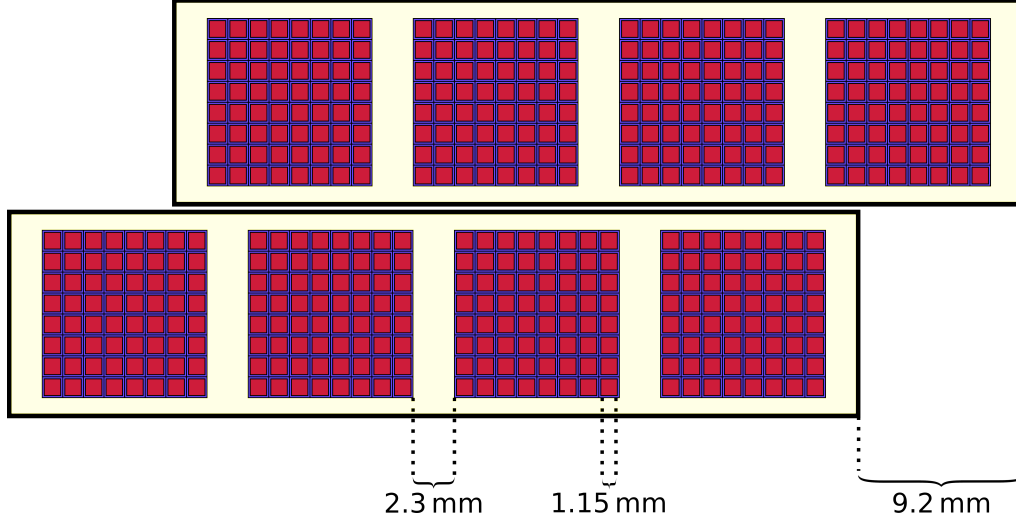


Figure 2.3: Schematic representation of two adjacent cassettes. The red squares depict the bins. The cassettes are placed with a slight offset to each other.

The offset between the two cassettes is important because in combination with the rotating gantry it extends the number of rings to 48. However this has the disadvantage of some area being covered by more bins than other areas. The product of number of rings with the number of bins per rings is 7680. This number may be doubled because of the phoswich concept leading to 15360 measuring points for the cylindrical FOV which has a ring diameter of 13.56 cm and a height of 11 cm. By closely investigating the values one finds a discrepancy between the height and the bin size in figure 2.3 which would be 1.15 mm. One expects that bin size times ring number equal approximately the height of the FOV. However 48 times 1.15 mm equals 55.2 mm. This discrepancy can be explained regarding the fact that 1.15 mm is the effective bin size. This is also depicted in figure 2.3 by placing the distance markings slightly narrower than the edges of the bins. The bin size in the experimental setup is 2.26 mm leading to the problem that only approximately a quarter of the utilized area is used in the reconstruction process. This may lead to inconsistencies in measurements as discussed in section 3.5.

There is an other possible error source. This would be the fact that LORs can exist in a way that they can not be detected because there is no intersection between LOR and bin. This effect is depicted in figure 2.4 and its importance increases with increasing closeness to the bases of the cylindrical FOV.

2.1.3 Homogeneous phantom

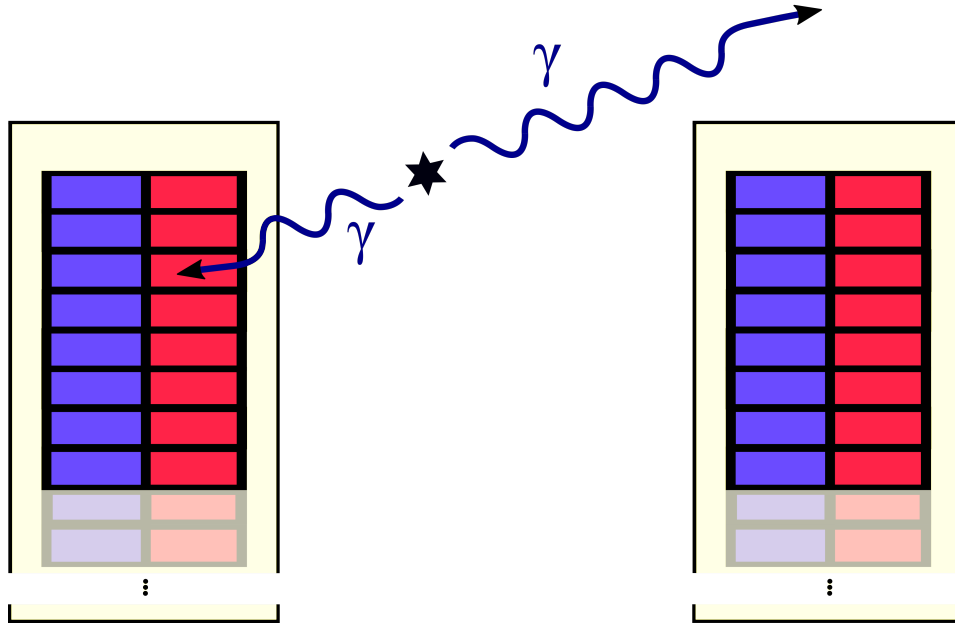


Figure 2.4: Schematics of the coronal plane of the FOV, depicting situation when only one out of two gamma rays is detected. In that case the LOR can not be reconstructed. Slightly transparent bins represent the possibly present bins when one considers the rotation of the gantry.

2.1.3 Homogeneous phantom

The homogeneous phantom as seen in figure 2.5, is handmade and includes the radioactive isotope Sodium-22 with an activity of 12 MBq instead of the usually used Fluorine-18.

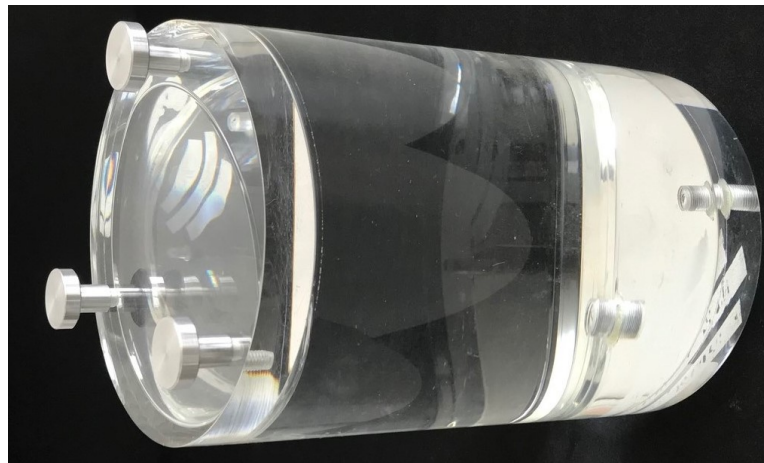


Figure 2.5: Homogeneous Sodium-22 phantom.

The usual procedure involves creating a Fluorine-18 solution. Because of the Fluorine-18 isotope's small half-life, long term radioactive contaminations can be almost excluded. The disadvantages on the other hand lay in the effort to provide a solution with Fluorine-18. Because of its small half-life one cannot store this isotope over a longer period of time. Another disadvantage is that this procedure includes the work with an open radioactive substance.

Therefore a closed radioactive substance has to be provided. This is the case for a homogeneous Sodium-22 phantom because it was glued with epoxy-resins which prevents the solution from leaking. This experimental setup has a further advantage in being very simple to handle because of the 2.6 years half-live of Sodium-22.

2.2 Physical background

Scattering is one possible interaction of photons with matter; other examples being the photo effect in which the photon transmits all of its energy to an electron that in turn leaves the atom it was bound to or pair production in which a photon interacts with the electromagnetic field of an atom to produce an electron-positron pair. As for scattering effects, further distinctions are to be made. On the one hand there is coherent scattering, the type of scattering where the incoming and the scattered wave are still coherent and thus can interfere with each other. An example would be Rayleigh scattering. On the other hand, there is incoherent scattering meaning the photon does transmit some of its energy leaving it with a now different frequency and thus the phase difference changes with time. Figure 2.7 shows that Compton scattering is an important interaction but also pair production is discussed. These phenomena and the occurring types of radiation are connected in section 2.2.4 to discuss the decay chain of the radioactive isotope Sodium-22.

2.2.1 Compton scattering

Compton scattering denotes a special model for incoherent scattering of a photon at a quasi-free electron, in which the electron is assumed to be a free electron, meaning no binding energy is present. Furthermore Compton scattering is a form of elastic scattering meaning that the sum of kinetic energies of the incoming particles versus the kinetic energies of the outgoing particles is conserved in the center of mass frame. The phenomenon of Compton scattering is depicted in figure 2.6 [6].

2.2.1 Compton scattering

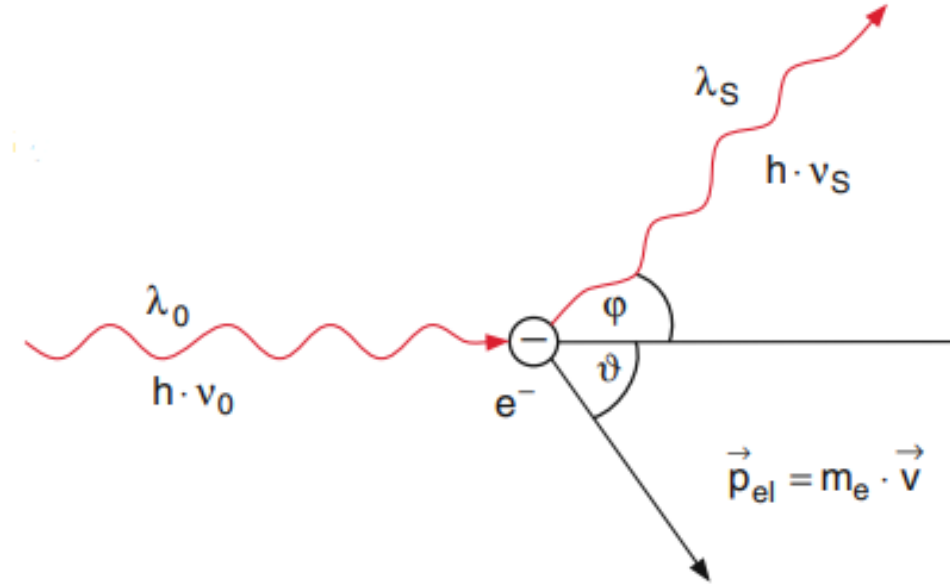


Figure 2.6: Kinematic of Compton scattering. An incoming photon with an Energy $E = h\nu_0$ is scattered at a free electron. The electrons momentum is noted as \vec{p}_{el} whereas the the photons energy decreases to $E = h\nu_S$. The photon is scattered with the angle φ which is the angle of interest for further considerations [6].

Using the prior assumptions, as well as treating the particles involved as particles instead of waves, the well-known formula for the Compton effect can be derived from energy and momentum conservation. Thus, the change in the wavelength of the photon is found to be in equation (2.1)

$$\lambda = \lambda_C \cdot (1 - \cos(\varphi)) \quad (2.1)$$

with the Compton wavelength λ_C and the scattering angle ϑ . This translates to the energy of the photon after the scattering to be

$$E(\mu) = \frac{E'}{1 + \kappa(1 - \mu)} \quad (2.2)$$

where $\kappa = \frac{E'}{E_e}$ is the ratio of the energy of the incoming photon and the rest energy of the electron and $\mu = \cos(\vartheta)$ is called the directional cosine.

Additionally the differential cross section is investigated. This gives us a statement which scattering angles most likely occur during Compton scattering. According to O. Klein and Y.

Nishina the differential cross section is to be found [7]

$$\sigma_{\Omega}^{KN}(\mu) = \frac{r_e^2}{2} \cdot \left(\frac{1}{1 + \kappa(1 - \mu)} \right)^2 \cdot \left(\kappa(1 - \mu) + \frac{1}{1 + \kappa(1 - \mu)} + \mu^2 \right) \quad (2.3)$$

with r_e being the classical electron radius. This, however, is an approximation as the electrons in this model are assumed to be free whereas indeed they are bound with a certain energy. It causes the real cross section for incoherent scattering to drop for sufficiently small scattering angles as not enough energy is being transmitted to the electrons. The angular dependence is represented in figure 2.7. For our considerations one investigates the distribution of the 511 keV line because this is the energy of the emitted photons (see section 2.2.4). One observes that photons can be scattered in all directions with a non-negligible probability. Therefore it is clear that Compton scattering should be considered as a serious source of error because it changes the direction of a photon and therefore invalidates the reconstruction.

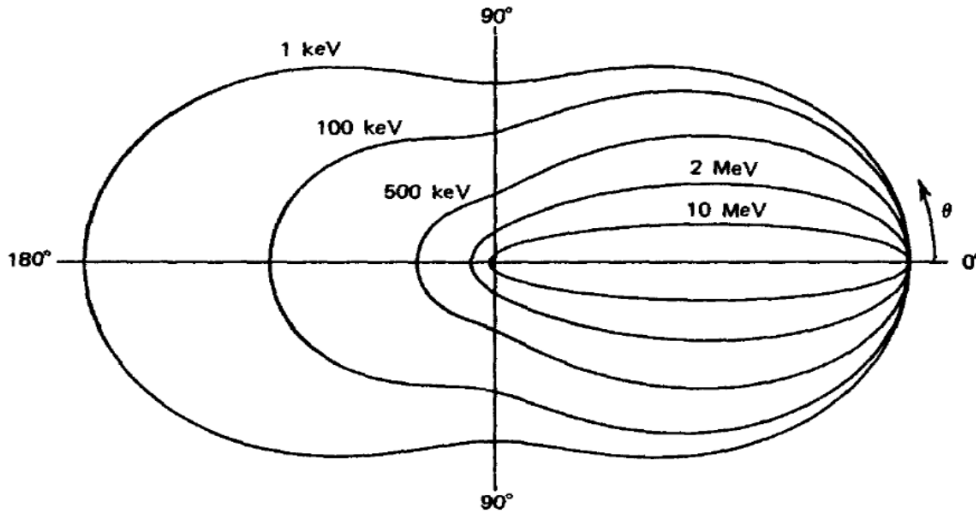


Figure 2.7: The Klein-Nishina differential cross-section distribution as a function of the scattering angle. The photon scattering probability is proportional to the distance from the plot center [8].

It is also important to understand the relationship between Compton scattering and the other interactions of photons with matter. Figure 2.8 represents the cross sections for interactions. One verifies that Compton scattering is dominant for energies about 511 keV in this experimental setup. This observation is important because it shows that Compton scattering is the most important interaction and therefore one focuses on it.

2.2.2 Attenuation coefficient

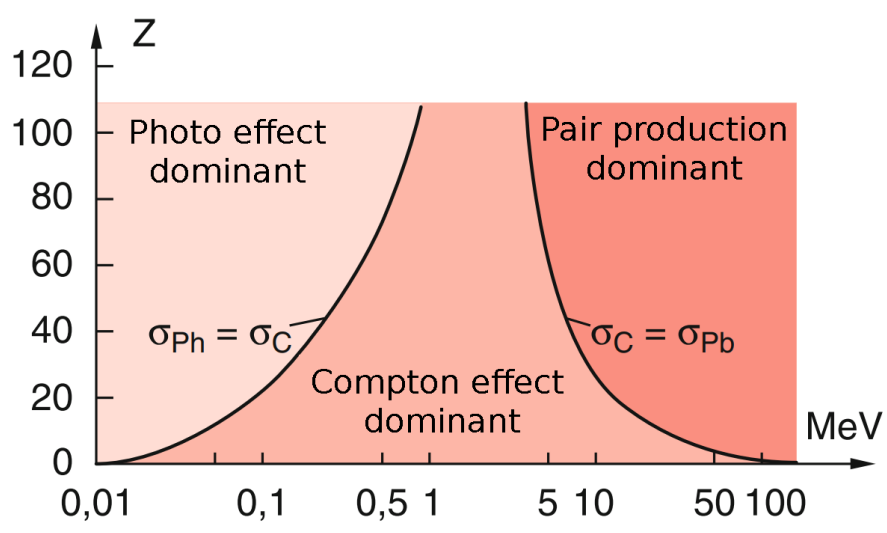


Figure 2.8: Different interactions of photons as a function of energy and atomic number. Because the scattering occurs mostly in the phantom and there is no substance with a higher atomic number than Sodium-22, one concludes that Compton scattering is a dominant scattering mechanism for the photons of 511 keV energy [7].

2.2.2 Attenuation coefficient

“The mass attenuation coefficient μ/ρ , of a material for uncharged particles of a given type and energy, is the quotient of dN/N by ρdl , where dN/N is the mean fraction of the particles that experience interactions in traversing a distance dl in the material of density” [9]. This definition is represented by equation (2.4)

$$\frac{\mu}{\rho} = \frac{1}{\rho dl} \frac{dN}{N} \quad (2.4)$$

The attenuation coefficient for water and photons of about 511 keV equals 0.096 cm^{-1} according to Thielemans et al. [10]. It is used in the reconstruction process utilizing Beers law as described later in section 2.3.1.

2.2.3 Types of radiation

Radioactivity can be considered as a property of instable nuclei. By emission of particles or energy an unstable nucleus transforms itself into a new nucleus or into a new state of energy. The types of radiation characterize the processes. The two occurring types of radiation in the measurements are γ and β radiation.

γ radiation requires an atom in an excited state of energy. Excited state means in this case that an electron is on a energy level which is not the lowest possible one. The radiation occurs

when the electron decreases its energy level initiating at the same time emission of the photon. The energy of the photon is

$$E = h \cdot \nu = h \cdot \frac{c}{\lambda} \quad (2.5)$$

with h being the Planck constant and ν the frequency of the photon when its considered as a wave. The photons frequency and therefore its energy represent the required degree of freedom to fulfill energy conservation in the emission process of γ rays.

β^+ radiation occurs when an atom emits a positron and a neutrino. The process can be described by equation (2.6)



where X and Y describe two different nuclides, e^+ a positron and ν_e the corresponding neutrino. β decay in general has an interesting property. Due to the neutrino there are three resulting particles after the decay. The emitted positrons energy possess spectral behavior because the momenta of the three particles are only restrained in two degrees of freedom by energy and momentum conservation [7].

2.2.4 Sodium-22 and related physical phenomena

Sodium-22 referred to as ${}^{22}\text{Na}$ is a β^+ emitter. When Sodium-22 decays, according to equation (2.6), a Neon-22 atom, a positron and a neutrino result.

Photon pair production

A positron annihilates with an electron to two photons. The occurrence of electrons is a requirement which is fulfilled because our measurement system does not include a vacuum. Now one investigates the annihilation process in the center of mass frame of the electron and positron. The process is visualized in figure 2.9.

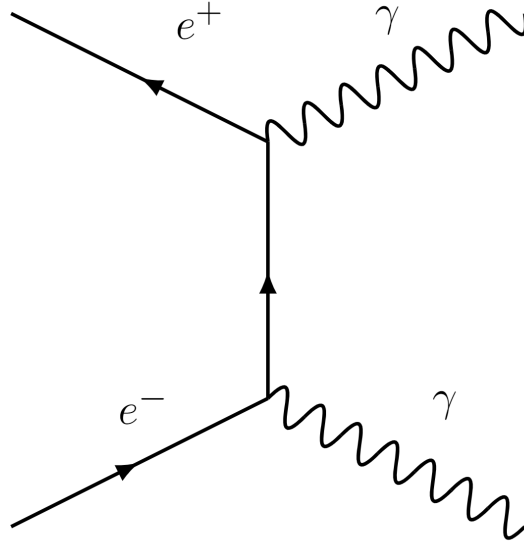


Figure 2.9: Feynman diagram of positron electron annihilation. Time propagates along the horizontal axis.

The incoming particles in the diagram are an electron and a positron and the outgoing particles are two photons. Before the reaction, one assumes that both particles have zero momentum. It follows from the momentum conservation law that two photons are emitted in opposite directions with a vectorial momentum of equal magnitude. The photons emitted in opposite directions produce a LOR. Because both particles are identical the only possibility to achieve equality of vector norms is to set the energies of the photons equal:

$$p_{\gamma_1} = p_{\gamma_2} = \frac{E}{c} = \frac{h}{\lambda} \quad (2.7)$$

Furthermore if one considers Einsteins mass energy relation in equation (2.8) with the electron rest mass:

$$2 \cdot E_{\gamma} = E_e + E_e = 2 \cdot m_e c^2 \quad (2.8)$$

One obtains an expected value of 511 keV as energy for the two emitted photons. These considerations form the basis of the reconstruction process.

The decay chain of Sodium-22

Figure 2.10 presents the decay chain of the Sodium-22 isotope [2].

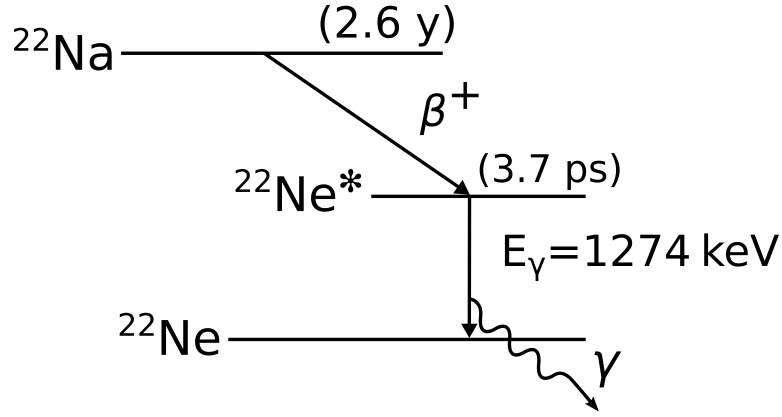


Figure 2.10: Decay-chain of Sodium-22 into Neon-22.

Since our measurement system works in energy windows below 750 keV, the 1274 keV γ radiation cannot be detected directly. This changes with consideration of the Compton scattering. Utilizing equation (2.2) with the current parameters one obtains figure 2.11 which shows that Compton scattered 1274 keV γ -rays can be detected by the detector. This observation is important because it represents an error source which cannot be prevented.

The scattering angles of at least 44.1° may distort the measurements because the LORs are

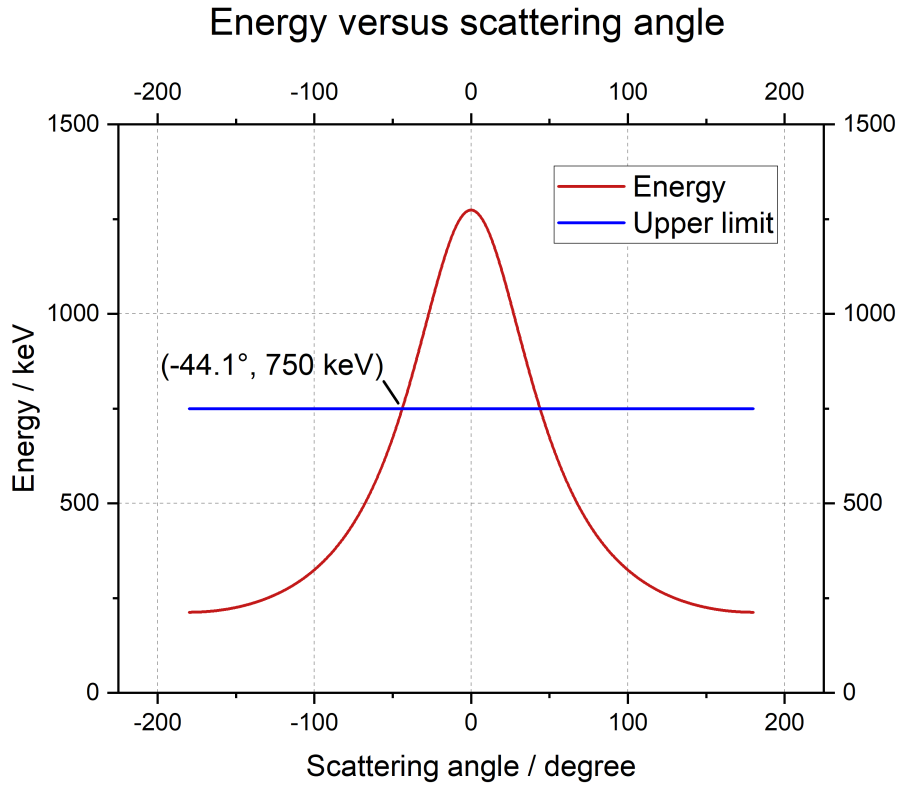


Figure 2.11: Energy of Neon-emitted γ ray after Compton scattering versus scattering angle. This shows that gamma rays which are Compton scattered by at least 44.1° may be detected by the measurement system.

only reconstructed based on the exited bins in the cassettes. The bigger the scattering angle the more the initial LOR differs from the reconstructed LOR. Therefore, even neglecting imperfection of the provided measuring system, a statistical behavior of every measurement is to be expected. It is clear from figure 2.7 that the photons of 1274 keV energy are scattered at all angles with non-negligible probabilities. However, at this high photon energy, the scattering happens preferentially at small angles.

2.3 Reconstruction process

This section focuses on providing the basic concept of the reconstruction process. It covers a description of the problem in section 2.3.2 and an analytical way to solve it. With the OSMAPOSL algorithm an iterative algorithm is presented in section 2.3.3 to counter the drawbacks of the analytical solution.

2.3.1 Intensity and Beer's law

Intensity The intensity is defined as noted in equation (2.9)

$$W = \int \mathbf{I} \cdot d\mathbf{A} \quad (2.9)$$

with W being the net power, \mathbf{I} being the intensity and $d\mathbf{A}$ being the infinitesimal surface element.

Beer's law “Each material has a characteristic linear attenuation coefficient μ for rays emitted at a given frequency” [11]. This is described in equation (2.10)

$$\frac{dI}{ds} = -\mu(x(s))I(s) \quad (2.10)$$

with s being the arc length along the trajectory described by the ray.

2.3.2 Radon transform and its inverse

By introducing the Radon transform one provides an analogy for all reconstruction processes. The Radon transform itself can be referred to as forward projection transforming the source activity distribution to a different space depending on angles and distances to the middle rather than spatial coordinates. If one omits the 3rd spatial dimension the location of the

LORs in the experiment can be described by one angle and their distance to the middle. This is formalized in equation (2.12). The inverse Radon transform representing the back projection would return the solution to spatial coordinates finishing the reconstruction process.

Now one can define the Radon transform $\mathcal{R}f : \mathbb{R} \times [0, \pi) \mapsto \mathbb{C}$ in equation (2.11) for a two dimensional problem with $f \in L^2(\mathbb{R}^2)$ according to Candes [12]:

$$\mathcal{R}f(t, \theta) = \int_{L_{t,\theta}} f(\mathbf{x}) dS(\mathbf{x}) = \int \int f(\mathbf{x}) \delta(\langle \mathbf{x}, \mathbf{n}_\theta \rangle - t) d\mathbf{x} \quad (2.11)$$

with $\mathbf{n}_\theta = (\cos \theta, \sin \theta)$ being the unit vector in the direction determined by θ . This definition is connected to our problem because the source activity distribution is described by f . $\mathcal{R}f$ is the integral of f along $L_{t,\theta}$ whose direction is perpendicular to \mathbf{n}_θ . The distance from the origin is t . $L_{t,\theta}$ is defined in equation (2.12). One could visualize equation (2.11) by marking the $\mathcal{R}f$ value of each (t, θ) pair with a color. The brighter the color the higher the value. This kind of diagram is called sinogram.

$$L_{t,\theta} = \{\mathbf{x} : \langle \mathbf{x}, \mathbf{n}_\theta \rangle = t\} \quad (2.12)$$

This definition is depicted in figure 2.12. It is to be noted that $L_{t,\theta}$ can be seen as a representation of a LOR.

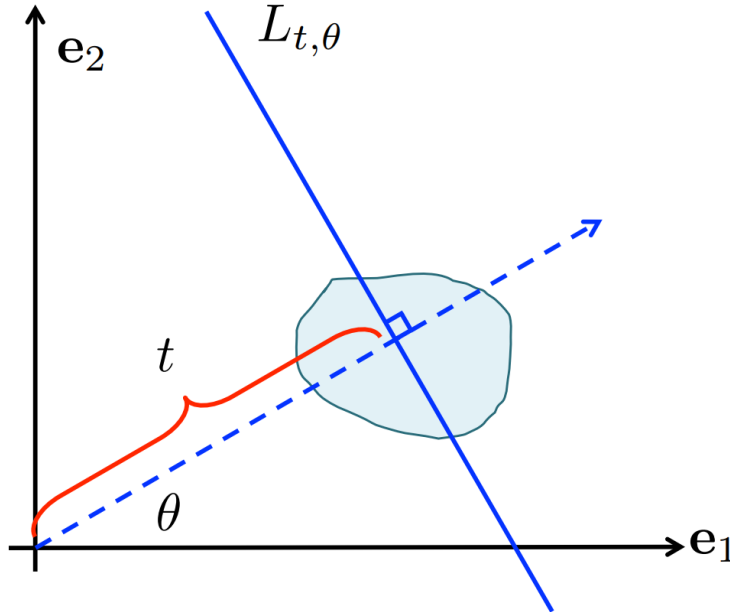


Figure 2.12: The Radon transform visualized. $L_{t,\theta}$ can clearly be seen as integration path over the green set which represents the function f with non zero values [12].

2.3.2 Radon transform and its inverse

Each value of f contributes to the integral. Therefore an intuitive definition of the backprojection would be to take an average of the Radon transform. This idea leads to equation (2.13),

$$\tilde{f}(\mathbf{x}) = \frac{1}{\pi} \int_0^\pi \mathcal{R}f(\langle \mathbf{x}, \mathbf{n}_\theta \rangle, \theta) d\theta \quad (2.13)$$

followed by a visual representation for an example reconstruction in figure 2.13. One can clearly see that the reconstructed picture is blurred out and not an identical illustration of the original.

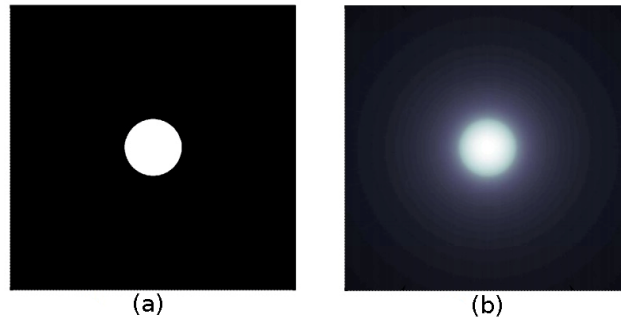


Figure 2.13: a) The initial image. b) Radon transformation and its inverse with occurring blur [12].

However, mathematical considerations as acquired by Candes [12] lead to the convolution theorem which represents the inverse Radon transform $\mathcal{R}^{-1} : L^2([0, \pi) \times \mathbb{R}) \rightarrow L^2(\mathbb{R}^2)$ and is slightly different than the back projection in equation (2.13).

$$f(\mathbf{x}) = \frac{1}{2\pi} \int_0^\pi (\mathcal{R}f(\cdot, \theta) * h)(\langle \mathbf{x}, \mathbf{n}_\theta \rangle) d\theta \quad (2.14)$$

With equation (2.14) one obtains the activity distribution from given LORs.

The equation is convoluted with h such that $\hat{h}(\omega) = |\omega|$. According to Candes [12] the problem is ill-posed meaning that small changes in the initial values, namely the sinograms may change the solution e.g. the reconstructed image by a not negligible amount. The idea behind this involves two steps.

1. The bins are discrete and therefore one needs to replace the integral with a sum.
2. The convolution of \mathcal{R} with h leads to the occurrence of a derivative if one keeps in mind that the Radon transform and its inverse are tightly connected to the Fourier space [12]. Equation (2.14) is basically a Fourier transformed value multiplied with $|\omega|$. Now one can utilize $\mathbb{F}(\frac{d}{dt}f(\omega)) = i\omega\mathbb{F}(f(\omega))$ with \mathbb{F} being the Fourier transformation. Considering

that one has discrete data points and compares values to some point which are similar to derivatives between discrete data points, it is clear that a small change in a point might change the derivative by a huge amount. Therefore the Radon inverse problem is ill posed. This is an explanation for blur and unexpected behavior during the back projection.

2.3.3 OSMAPOSL algorithm

It was shown in section 2.3.2 that a back projection needs further enhancement for production of clear reconstructed data. The Ordered Subset Maximum A Posteriori One-Step Late (OSMAPOS�) algorithm is an iterative algorithm to for data back projection. It is an advanced version of the One Step Late algorithm [10]. Before starting a detailed explanation it is necessary to define some terms:

- A **voxel** is one pixel in the three dimensional coordinate space. Each voxel has a value proportional to the reconstructed activity at this coordinate. The values of voxels can be depicted in activity images or be considered in line profiles which are used in this thesis to present the results.
- A **segment** is referred to as the ring difference between the bins which detect a LOR. The allowed ring difference in the measuring system range from -15 to 15. In the reconstruction process LORs are grouped according to their segment. Segments allow to reduce the reconstruction from a three dimensional problem to a two dimensional problem for each segment and each ring.

The OSMAPOSL algorithm has implemented following features:

Sensitivity image The sensitivity image is the main part of the OSMAPOSL algorithm. Its idea is to measure a homogeneous activity over the whole FOV. This activity image is referred to as normalization. If one preserves a new reconstruction the reconstructed voxels are multiplied with the inverse value of the voxels from the normalization. This has the following advantage. Assume a voxel has different values than the adjacent voxels, because there may be bad or not working bins in the cassettes hampering the reconstruction process. Then this voxel has different values in both measurements: In the actual one and in the normalization measurement. The idea is that by multiplying the voxels value with the inverse of the voxels value from the normalization, these errors cancel out.

The Cartesian Metz filter “This is a separable 3D Metz filter for images discretised on a Cartesian voxel grid. These filters are composed of 3 1D filter kernels, one for the x,y and z directions each. Each 1D filter is specified by a Full Width at Half Maximum (FWHM)

parameter (in millimetres), Metz power parameter and maximum spatial kernel width.” [10]. Further discussion by Jacobson et al. [13].

Parameters The most important parameters to be considered is the number of subsets. Subsets were introduced to divide the computational tasks in simpler ones. The more subsets the simpler the tasks leading to the drawback of decreasing image quality. It was decided to use the OSMAPOS algorithm with only one subset to achieve the best possible results.

A further parameter is the number of subiterations. Because the OSMAPOS is an iterative algorithm it tries to approach values for each voxel, which correspond well with the normalization measurement. The more subiterations the more computational power required but also the better the results. According to Bettinardi et al. [14] ten iterations is a number which leads to satisfactory results.

2.4 Fourier rebinning algorithm

A rebinning algorithm is an algorithm which sorts data from a 3 dimensional set to a 2 dimensional set. The only allowed segment is 0 after applying a rebinning algorithm. For detailed information see Defrise et al. [15].

3 Experimental results

In every experimental thesis measurements and their interpretation are the core part of interest. In this work one investigates point sources and tries to improve the reconstruction procedure under consideration of statistical parameters. These contemplations focus on source activities in different areas of the scanner. First of all one clarifies the task regarding this measuring system. It was required to upgrade the reconstruction software STIR. The computer found at the beginning of the working period utilized STIR version 1 whereas the current STIR version is 4.1.0 which was released in 2021. Because of outdated software and hardware restrictions one decided to reproduce the reconstruction process on a different device which suits latest requirements of software and hardware. Reproducing the system with a completely new STIR version, manufacturing backups from hard drives and many other non physics related steps had to be done to upgrade the whole system, thoroughly test it and obtain the desired results.

The two point sources utilized in this work are ^{22}Na sources with different activities. Measurements and formulas regarding the source with the higher activity, will be indexed with a “ $_s$ ” (s for strong) whereas measurements and formulas with the lower activity will be indexed with a “ $_w$ ” (w for weak). Following activities are given without an error beyond the uncertainty of the unknown digits:

$$A_s = 232 \text{ kBq} \tag{3.1}$$

$$A_w = 38.7 \text{ kBq} \tag{3.2}$$

There is one further remark about the ClearPET which is necessary to take into account during the measurements. The ClearPET currently has a not fully functioning cassette. As shown in figure 3.1 the cassette twelve does not perceive any events. The affected blocks are adjacent and cover the area reaching from the cassettes edge to its middle. For further measurements this is a subordinate factor because one measured in FOVs which do not include areas analysed by not working parts of the detector.

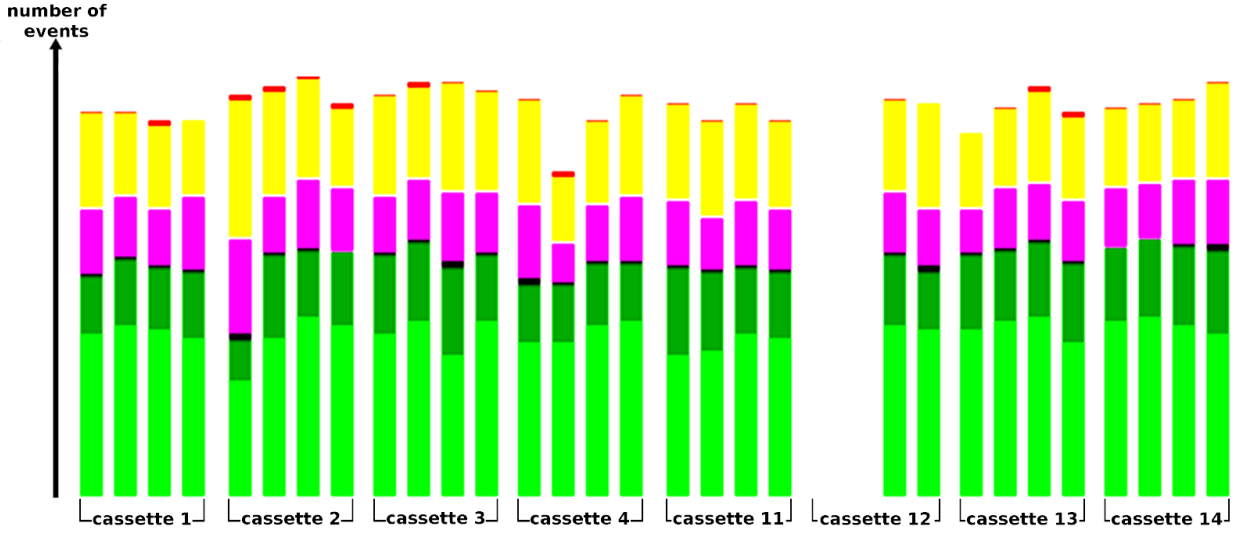


Figure 3.1: Number of events for different cassettes. The light green bar depicts single hits, dark green shows neighboring hits, black represents positional errors, pink depicts multiple hits, yellow shows energy errors, red represents other errors. Further discussion by Lehr [4].

3.1 Reconstruction routine

After obtaining the binary measurement data in the preprocessors there are two steps implemented. One needs to call the function for “coincidence sorting” which processes the detected events and combines them with an angular position file. This is necessary because as mentioned in section 2.1 the gantry rotates which leads to a time dependant location of the cassettes. The output of this function is a binary file. One needs to convert this binary file to the interfile format which is used by STIR. This is achieved by the “rebinning” function. Both functions were provided by the manufacturers of the ClearPET. After these two steps one uses the STIR reconstruction software. The reconstruction process is implemented in python and is shown in the appendix.

It is important to note that the rebinning algorithm provided by the manufacturers differs from those provided by STIR. According to Thielemans et al. [10] a rebinning algorithm should reduce the number of segments to one. However, this is not the case after applying the rebinning algorithm of the manufacturers. This problem can be solved with the FORE algorithm (see section 2.4) which allows reduction of segment’s number after the manufacturer’s procedure is applied.

3.2 Back projection of point sources

In this section the back projection of point sources is investigated. The reconstruction yields the following charts shown in figure 3.2. Note that these charts are not suitable for a

quantitative analysis because the color intensity is normalized in a way that the full spectrum is used. Manually adjust the spectra would be deceptive and is therefore neglected. The data was measured for an energy window from 250 keV to 750 keV. The measurement time amounts four minutes.

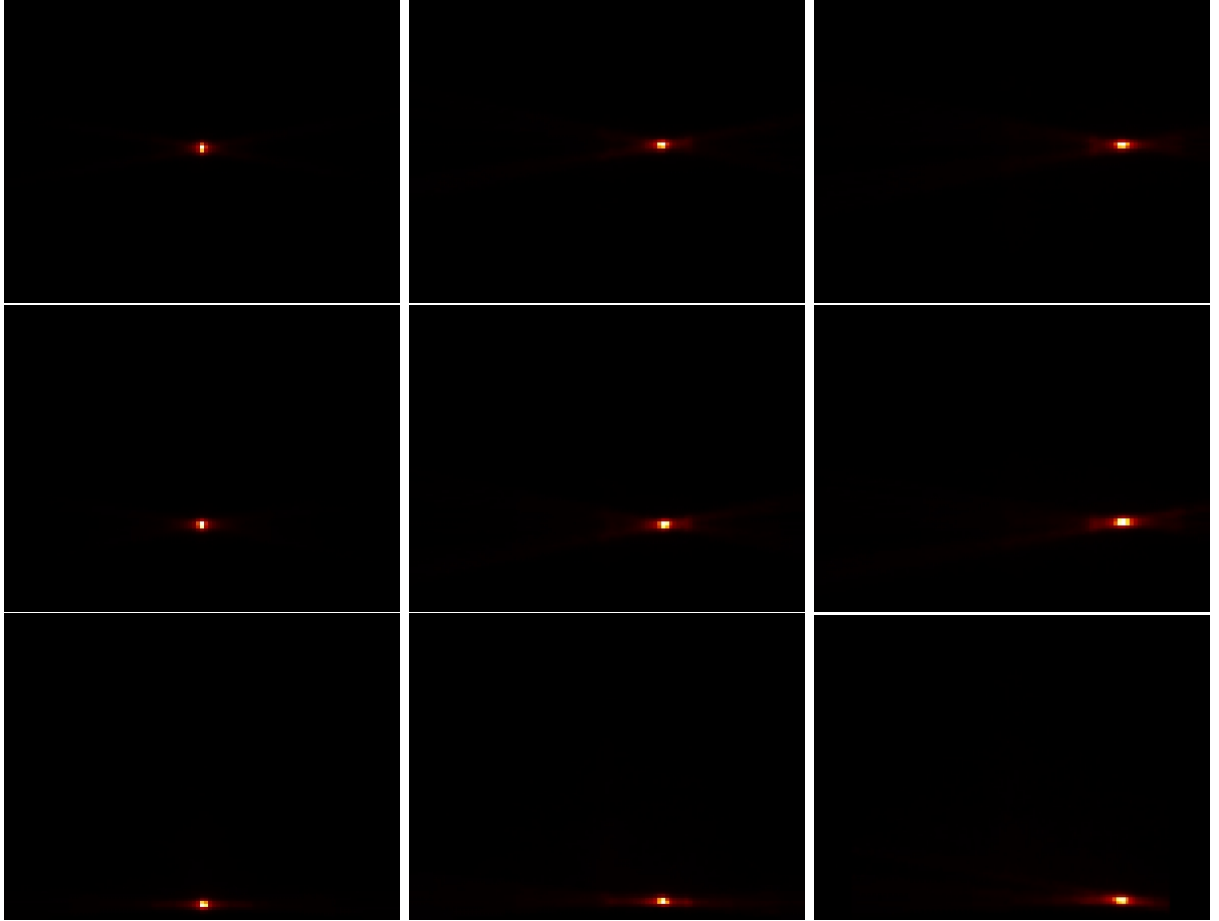


Figure 3.2: Reconstruction in the coronal plane of the strong point source in different positions. The x and y axes in the pictures represent the transverse and the axial axes of the FOV respectively. The transverse distance from the middle of the detector increases row by row and the axial distance from the middle increases line by line. The color represents the intensity of the depicted voxel. It increases from black over red to white.

The measurements do not include the upper part in axial direction because of the broken cassette, as described in section 2.1.2. Additionally, in transverse direction it is sufficient to investigate the dependance of activity versus distance from the middle because of the cylindrical symmetry. Due to the rotation of the gantry measurements in a different transverse position with the same distance to the middle would lead to the same result. Therefore there are no measurements in the left side of the pictures. From now on the “distance to the middle” is referred to as an offset.

Analysis of figure 3.2 shows two important systematic tendencies:

- There is blur in transverse direction.
- The blur increases with increasing transverse and axial offset.

Although in general the blur is expected (see discussion in section 2.3.2), it is asymmetric and requires further quantitative consideration of the problem and optimization of the whole reconstruction process.

3.2.1 Full width half maximum analysis of the strong point source

First of all one extracted the intensities along a horizontal line, as seen in figure 3.3 and investigated intensity values along the horizontal turquoise line because the blur occurs along the transverse direction.

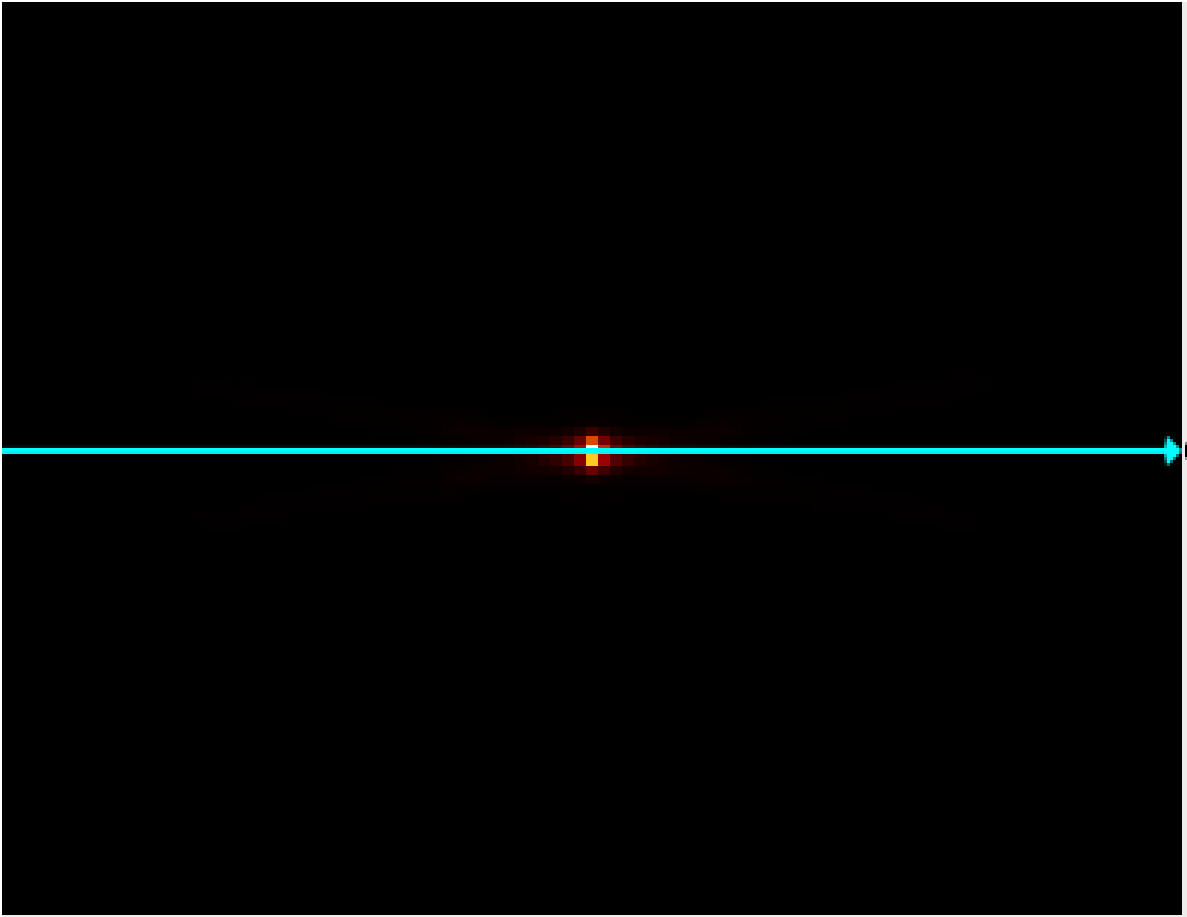


Figure 3.3: Chart for point source without offset from figure 3.2. Intensity values along the turquoise line are taken in further statistical analysis.

At first glance one might consider this procedure incorrect because the location of the line determined by the experimenter seems subjective. However, due to the low resolution there is one unique position for the line which includes the maxima. With this data one could perform a Gaussian fit, see figure 3.4. The Gaussian fit is utilized because it allows the determination

3.2.2 Investigation of the statistical error

of FWHM values. These values are an objective description of the width of the intensity spectrum. It is to be noted that one does not know the unit of the intensity. Because different algorithms use different reconstruction methods the intensity values between different figures can not be compared. To describe this interrelations one uses the term “arbitrary unit”.

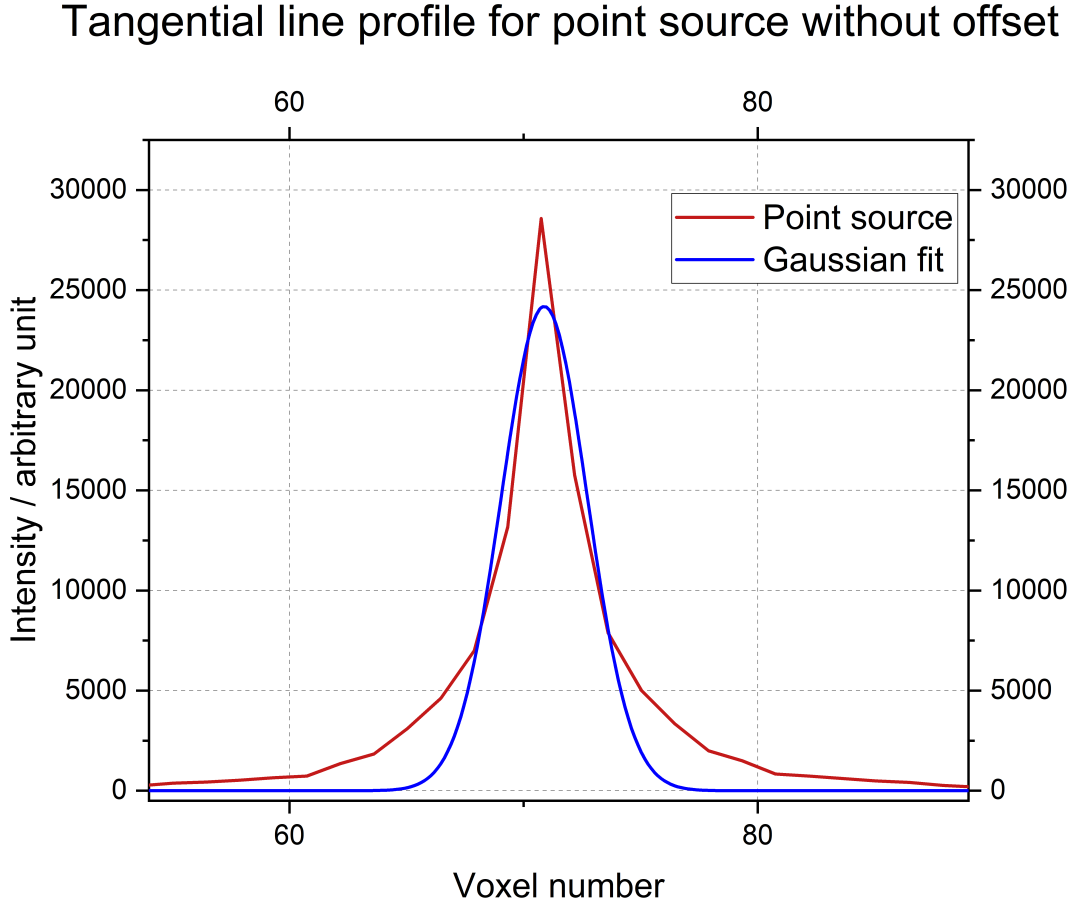


Figure 3.4: Transversal line profile for point source without axial and transverse offset and its Gaussian fit.

The analysis shows that the Gaussian fit underestimates the maxima and visually does not describe the line profile well. The measured intensity spectrum is not satisfactory because a point sources activity is sharply delineated whereas the measured spectrum is not. It is noisy and requires improvement of the reconstruction process. The FWHM for the different point source positions are summarized in table 3.1. Note that the measured data confirms the observation of increasing blur with increasing offsets in both axial and transverse direction.

3.2.2 Investigation of the statistical error

Because the coloring is normed one needs a different approach than the visual comparison to deal with source activities. The intensity is proportional to the density of events. To obtain

Table 3.1: FWHM values for different offsets. The arrangement of the FWHM values equals the arrangement of the charts in figure 3.2.

		transverse offset /mm		
		0	20	40
axial offset /mm	0	4.31	6.32	7.51
	25	4.44	7.28	8.50
	50	4.62	8.85	9.31

a number proportional to the number of events one usually would sum all the voxel values up. STIR provides utilities to do so. However, this approach does not provide satisfactory results because it takes all the noise, as seen in figure 3.4, into account. Therefore the maximal values of each peak are considered. This approach uses the fact that our voxel size is a constant between different charts. Moreover the assumption of sufficient events is made which means that the event's number is still large enough that the statistical errors do not dominate.

3.2.3 Validation of the maxima approach

It is to be approved that four minutes of measurement time is sufficient when using an energy window from 250 keV to 750 keV. For this purpose five measurements of the weak point source without offset have been taken. Their results can be investigated in table 3.2.

Table 3.2: Maximum values of different measurements for the weak point source in an arbitrary unit.

maximal value	3351	3359	3409	3416	3356
---------------	------	------	------	------	------

Now one can perform a statistical investigation and obtain the values provided in equations (3.3) to (3.5). It is noteworthy that one cannot perform an error contemplation using Poisson statistics because one does not know how the number in table 3.2 is computed.

$$\text{standard deviation:} \quad \sigma = 31 \quad (3.3)$$

$$\text{mean value:} \quad \mu = 3378 \quad (3.4)$$

$$\text{relative statistical error:} \quad \frac{\sigma}{\mu} = 0.9\% \quad (3.5)$$

Regarding the relative error of below 1% for the weak source one can see that the maxima approach is valid.

3.3 Comparison of activities and quantification of spatial reconstruction behavior

As mentioned earlier the maxima of the event density is proportional to the activities. The degree of freedom of the proportionality factor has to be eliminated by providing a known source. This is achieved by comparing the maxima ratio with the theoretically determined ratio of the strong and the weak point source. For this purpose the measurements, as visualized in figure 3.2, are repeated for the weak point source. Furthermore one examines the ratios of the maxima of the same point source and their normalization coefficients. Normalization coefficients, abbreviated as “Norm”, mean the ratio of the maxima in the current described position versus the maxima in the position with the same axial offset but different transverse offset. The results are presented in table 3.3.

Table 3.3: Activity ratio and normalization coefficients for different positions in the FOV.

axial offset/mm	transverse offset/mm	Activity ratio	Norm _s	Norm _w
50	0	0.140	1	1
	20	0.167	0.457	0.543
	40	0.169	0.316	0.380
25	0	0.182	1	1
	20	0.174	0.421	0.402
	40	0.219	0.216	0.260
0	0	0.136	1	1
	20	0.181	0.301	0.399
	40	0.188	0.180	0.248

First the theoretical values have to be compared with the computed ones. Statistical investigation lead to following result:

$$\text{experimental activity ratio:} \quad r_{exp} = 0.172 \quad (3.6)$$

$$\text{theoretical activity ratio:} \quad r_{th} = 0.167 \quad (3.7)$$

$$\text{standard deviation:} \quad \sigma_{exp} = 0.025 \quad (3.8)$$

$$\text{relative statistical error:} \quad \frac{\sigma_{exp}}{r_{exp}} = 14 \% \quad (3.9)$$

One can clearly see that the back projection is suitable to reconstruct known activity relationships because the theoretical value is inside the error boundaries of the experimental value and its errors. The relative error of 14 % is acceptable regarding the measurement system. However, the normalization coefficients are not. The deviation of activity which occurred by simply moving the source outside the middle made the activity of the same source differ by

a factor of up to five. Compton scattering in air, although could be one of the error sources, most likely makes an inferior influence. Likewise the attenuation coefficient of air. For the axial offset one could argue with the not detected LORs as discussed in section 2.1.2 but for the changes in transverse direction there is no explanation apart from strange reconstruction behavior. At this point the only available possibility is to pursue the ClearPET manufacturers approach and normalize the areas with high transverse offset by a factor which is determined from a normalization measurement for each voxel because the reconstruction process seems to treat bins different when their axial and transverse offset changes.

3.4 Normalization measurement

The normalization measurement was performed with the phantom as discussed in section 2.1.3 in an energy window from 250 keV to 750 keV over a time period of four minutes. After the measurement was finished, the reconstruction of the normalization was done utilizing a back projection yielding figure 3.5. For these images one observes three phenomena:

- The intensity decreases with increasing transverse offset. This observation is consistent with the observation that for increasing offsets the normalization coefficients, as seen in table 3.3 go down. The normalization measurement may solve this behavior, because during the reconstruction with the OSMAPOS algorithm each voxels value is multiplied with the inverse of the corresponding voxel value of the normalization measurement. However, the normalization measurement may be falsified by Compton scattering and attenuation of the γ rays.
- Ring structures are clearly visible. These exist because of the cylindrical symmetry of the detector and the phantom and are therefore expected.
- The intensity goes down at the top and bottom edges of the detector. This can be explained by not detected LORs as described in section 2.1.2.

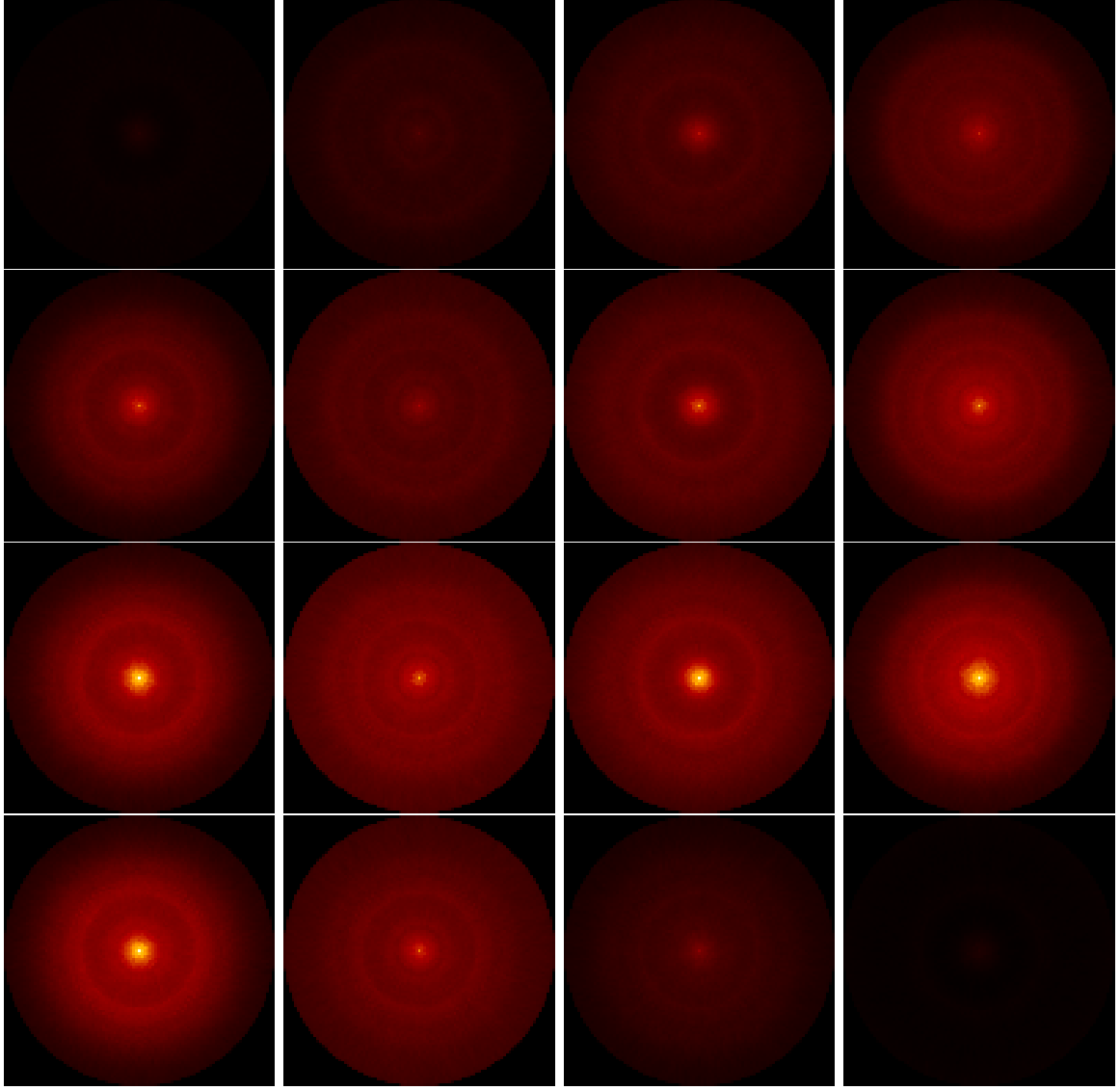


Figure 3.5: Back projection of the normalization measurement along the transverse planes. The distance of two adjacent planes is 7 mm. The distance from the first plane and the base of the phantom and the distance from the last plane to the base is 3 mm. The order of the planes is from left to right and from top to bottom.

As a different approach to reconstruct the normalized cylinder, the two dimensional filtered back projection algorithm without applying any external filters is investigated. The result is shown in figure 3.6. The artifacts may occur because of some algorithm implementation issues according to Thielemans et al. [10]. One can see that the activity of the phantom which has a homogeneous activity is depicted at the very low part of the spectrum meaning there are some black areas which should not be there. Unfortunately this behavior excludes the filtered back projection algorithm from further utilization because in the normalization one wants to divide each voxel with the corresponding voxel value of the normalization measurement. If the values change arbitrarily the normalization measurement misses its purpose. It might seem that the image quality is not sufficient but this is only the case because the distribution of

intensity has only a few very intense voxels in the middle. This can be observed especially in the second column of figure 3.6.

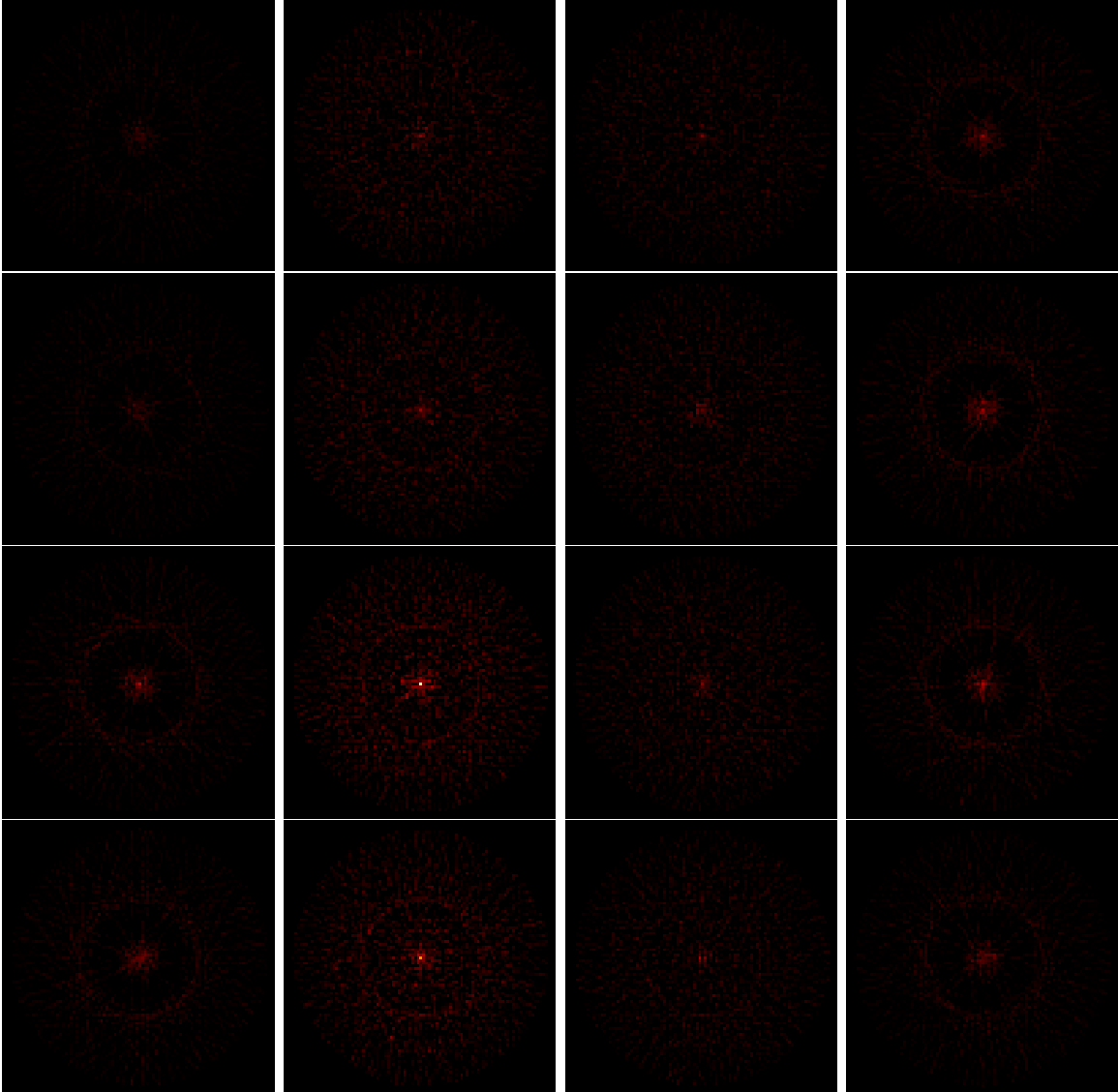


Figure 3.6: Two dimensional filtered back projection of the normalization measurement along the transverse planes. The distance of two adjacent projected planes is 7 mm. The distance from the first plane and the base of the phantom and the distance from the last plane to the base is 3 mm. The order of the planes is from left to right and from top to bottom.

3.5 Sinogram

Sinograms are results of the Radon transform, as discussed in section 2.3.2. They are a core concept of image reconstruction and represent the output of the detector after preparing the data with the applications provided by the ClearPETs manufacturers and the input of reconstruction processes for STIR utilities. By looking at sinograms one can investigate if the

provided measuring system works properly or if the data provided even before starting the reconstruction process is corrupted.

For this purpose the FORE is utilized to prepare the data. Its task is simple and well defined: The reduction of segments to one. Before applying the Fore one had 31 segments. As described in section 2.3.3, segments are the ring difference between two LORs. This would force us to analyse 31 one data sets, each containing a two dimensional representation of the Radon transform of the measured data for each value of z . Therefore the reduction to one segment is crucial. After this step one can easily extract the sinograms from the normalization measurement as seen in figure 3.7.

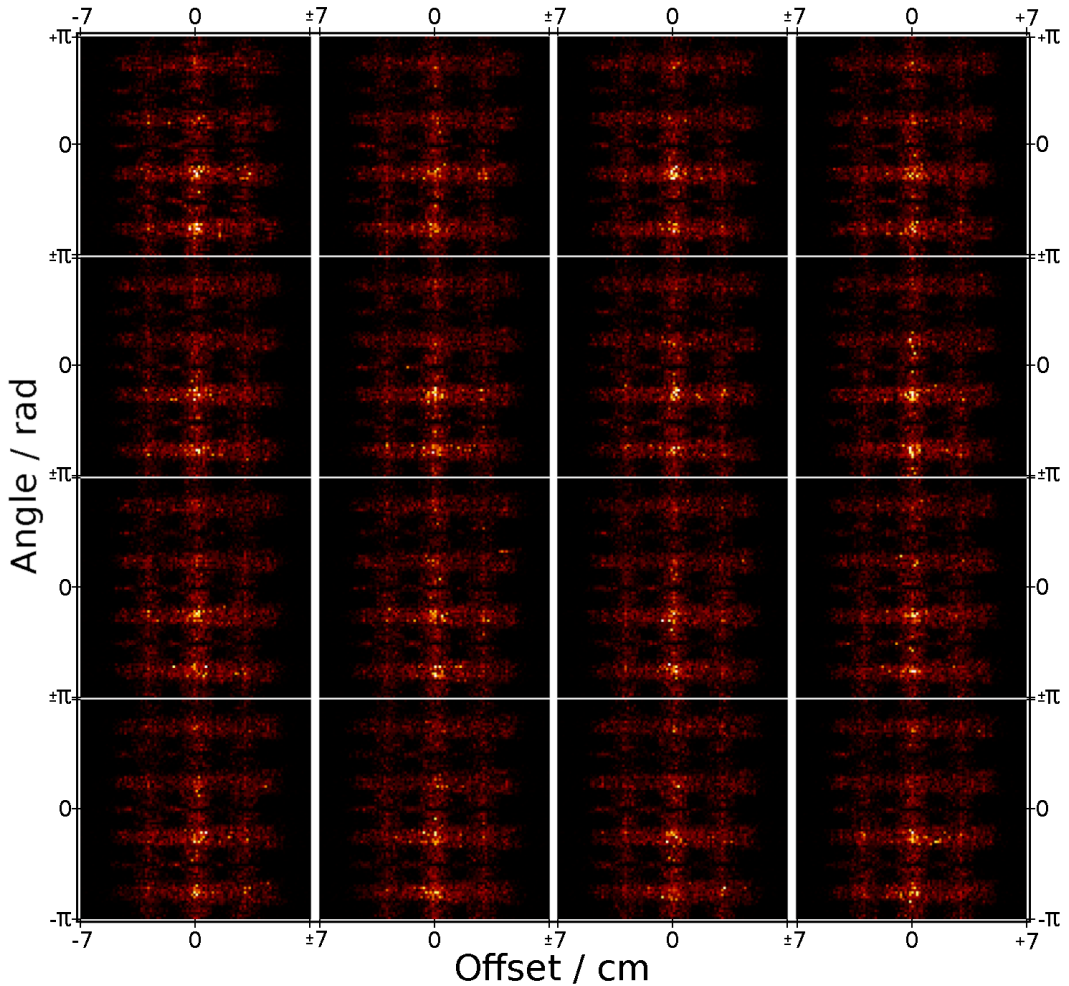


Figure 3.7: Sinograms in the transverse planes. The x-axis represents the offset, and the y-axis represents the angular dependency. The distance of sinograms of two adjacent planes is 7 mm.

First of all one expects to have no differences between the planes which is clearly the case. This is an important observation because it excludes statistical fluctuations as source of error.

Additionally no angular dependency is to be expected because there is a cylindrical symmetry for both the detector and the phantom due to the rotation of the gantry. Furthermore there are also problems considering the offset of the sinograms. One expects monotone and continuous decreasing intensity when moving from the middle to the edges because having a homogeneous activity implies that different values in a sinogram are obtained by shorting the integration path with non zero activity values rather than differences in the activity itself. This is a strong contradiction regarding the black areas. Also the discussed sources of error, in particular Compton scattering in section 2.2.1 or the attenuation of rays in section 2.2.2 do not explain this behavior because their impact changes also monotone in regard of transverse offset.

An approach to explain this behavior is to regard the scanners geometry. There are four blocks of eight times eight bins in transverse direction in each cassette. Concerning the behavior in terms of angular dependency, namely development along the y-axis, one observes four stripes. The distance between the bins also has an impact. As discussed in section 2.1.2 the effective bin area differs from the actual bin area by a factor of four. If the rays are not detected because of the effective bin area being smaller, it would explain the presence of black areas.

Another geometrical reason is the shift of the cassettes compared to each other. The shift compensates for the distances between the blocks. Nevertheless the distance exists and may be reason for incorrect sinograms. There is also a distance between two cassettes which could lead to corrupted data regarding the angle.

One can conclude that the data which is produced by the ClearPET is faulty. The deviations differ from what one would expect considering Compton scattering and the attenuation of γ rays. Inconsistencies of spatial activity behavior may be originated in the experimental setup rather than the reconstruction process. But this does not lead necessarily to bad results when one applies the OSMAPOSL algorithm because the voxels with less activity are normed that their importance increases as discussed in section 2.3.3. Hence the next step is to implement the OSMAPOSL algorithm and investigate its behavior.

3.6 Reconstruction with the OSMAPOSL algorithm

After reproducing the reconstruction process independently without software or hardware restrictions of the given measurement system, one implemented the reconstruction with the OSMAPOSL algorithm. First the OSMAPOSL algorithm is applied with one iteration for measurements with an energy window from 250 keV to 750 keV and measuring time of four minutes. This is the most basic execution of the OSMAPOSL algorithm. The reconstructed activities are shown in figure 3.8.

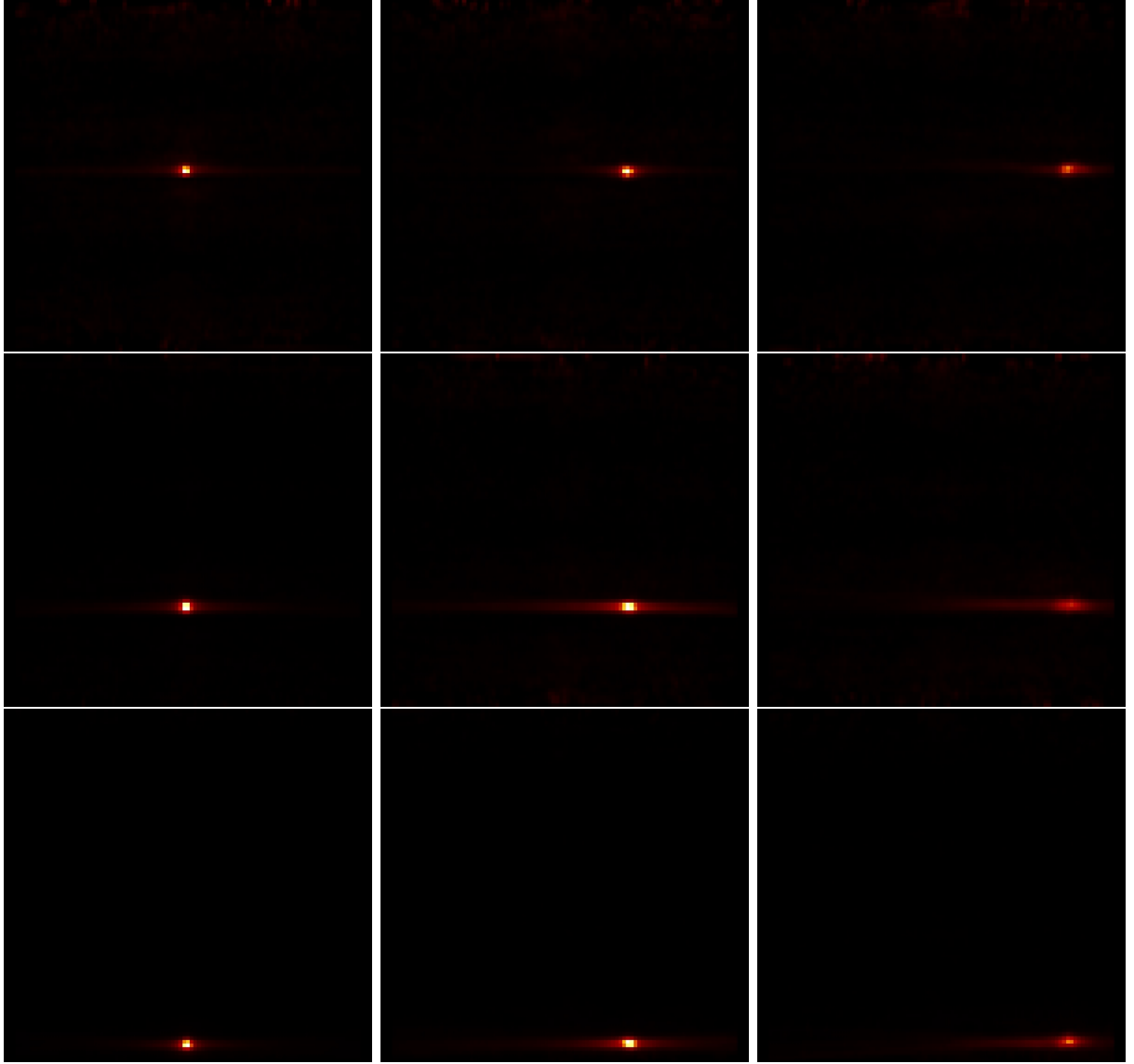


Figure 3.8: Reconstruction in the coronal plane of the strong point source in different positions. The x and y axes in the pictures represent the transverse and the axial axes of the FOV respectively. The transverse distance from the middle of the detector increases row by row and the axial distance from the middle increases line by line. The color represents the intensity of the depict voxel. It increases from black over red to white.

One sees that the blur is still present. This lets us assume that further improvements are necessary regarding the OSMAPOSL algorithm. Table 3.4 summarizes peak and blurring analysis of the OSMAPOSL experimental data using Gaussian fits. One observes for the FWHM behavior a slight improvement compared to the back projection analysed in table 3.1. Also the behavior with changing transverse offset stabilized for axial offset equal zero, see table 3.5. It is expected that values with increasing axial offset have increased susceptibility to errors because LORs may not be detected, as discussed in section 2.1.2. This effect can be verified by closely looking at the top or bottom edge of a activity image and observing noise. Equations (3.10) to (3.13) lead to the conclusion that interrelations between source activities

are reproduced correctly. Despite the good results one should definitely not overestimate them because the OSMAPOS algorithm is an iterative algorithm and needs more than one iteration to work properly. However, the measured data is much smoother than then in figure 3.3.

Table 3.4: FWHM values for different offsets.

		transverse offset /mm		
		0	20	40
axial offset /mm	0	3.79	4.96	6.29
	25	4.36	8.99	8.54
	50	4.39	8.77	7.42

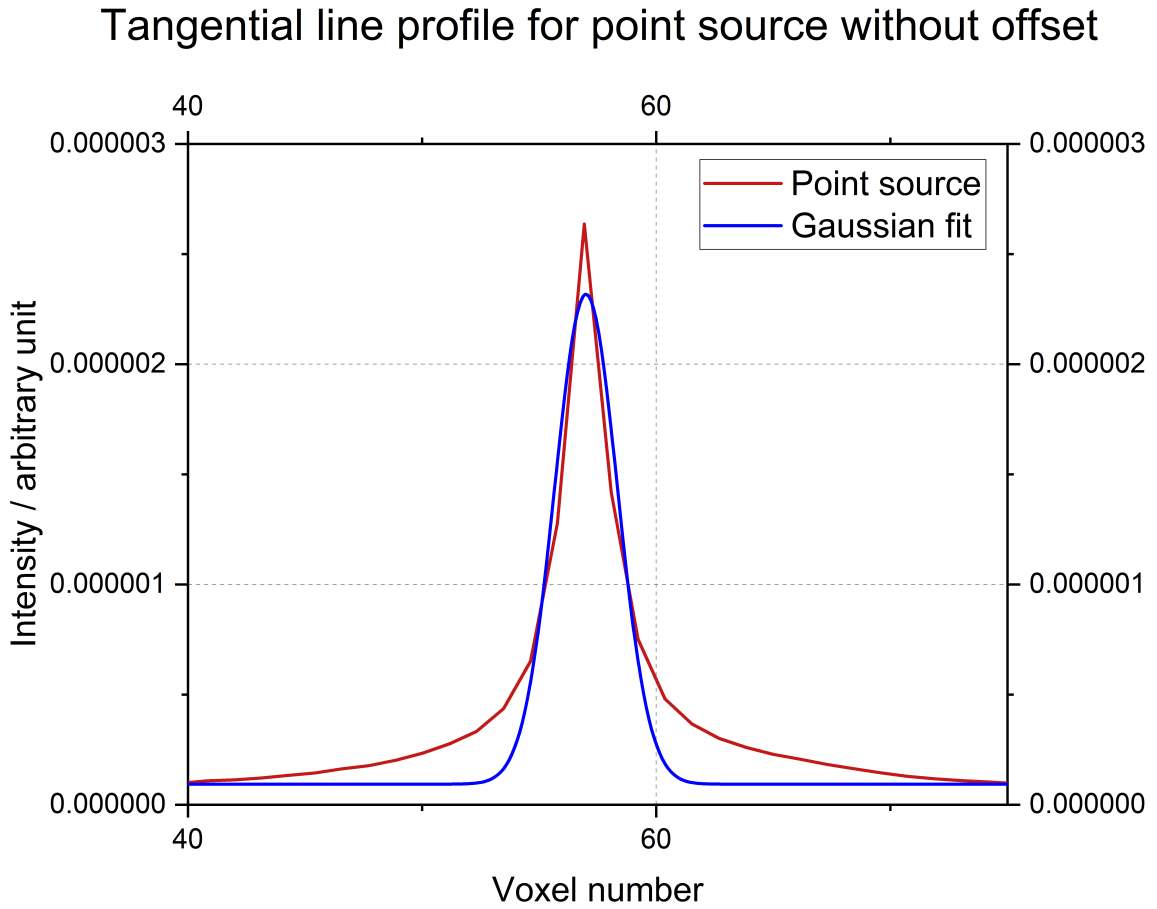


Figure 3.9: Transversal line profile for point source without transverse and axial offset and its Gaussian fit.

Table 3.5: Activity ratio and normalization coefficients for different positions in the FOV.

axial offset/mm	transverse offset/mm	Activity ratio	Norm _s	Norm _w
50	0	0.147	1	1
	20	0.203	0.289	0.399
	40	0.189	0.227	0.290
25	0	0.177	1	1
	20	0.166	0.447	0.420
	40	0.176	0.368	0.368
0	0	0.164	1	1
	20	0.167	1.13	1.15
	40	0.166	1.24	1.25

$$\text{experimental activity ratio:} \quad r_{exp} = 0.172 \quad (3.10)$$

$$\text{theoretical activity ratio:} \quad r_{th} = 0.167 \quad (3.11)$$

$$\text{standard deviation:} \quad \sigma_{exp} = 0.016 \quad (3.12)$$

$$\text{relative statistical error:} \quad \frac{\sigma_{exp}}{r_{exp}} = 10 \% \quad (3.13)$$

3.7 Implementation of attenuation correction and multiple iterations of the OSMAPOS�-algorithm

Attenuation of γ -rays occurs in the homogeneous phantom more frequently than in air because the average attenuation coefficient of water is lower. It is crucial to consider this fact. This was achieved by modeling a cylindrical phantom with STIR utilities. Each voxels value of the phantoms model amounts $\mu = 0.096 \text{ cm}^{-1}$. The attenuation correction factors were found by multiplying the result with -1, and afterwards applying Beers law, as discussed in section 2.3.1. Furthermore the number of iterations was increased from one to ten. This is an important step, because the OSMAPOS� algorithm is an iterative algorithm and approaches the solution iteratively. Figure 3.10 shows the corresponding reconstruction images.

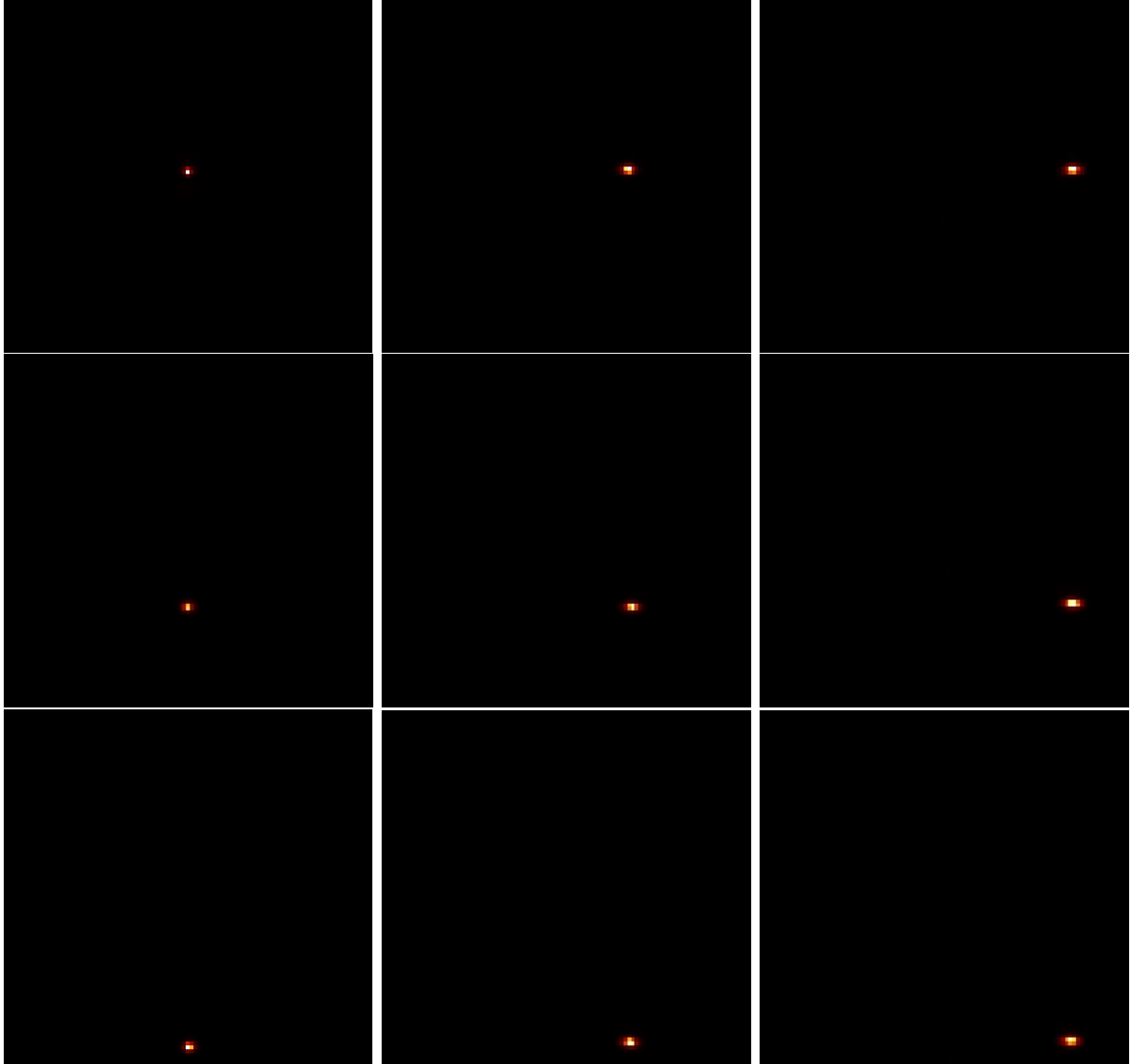


Figure 3.10: Reconstruction in the coronal plane of the strong point sources in different positions. The x and y axes in the pictures represent the transverse and the axial axes of the FOV respectively. The transverse distance from the middle of the detector increases row by row and the axial distance from the middle increases line by line. The color represents the intensity of the depict voxel. It increases from black over red to white.

One clearly can see that the blur disappeared. This is an improvement of the reconstruction process because the point sources now can be observed as clear points rather than a blear accumulation of events. It is to be investigated if this visual improvement can be quantized by the FWHM analysis as seen in table 3.6.

Table 3.6: FWHM values for different offsets.

		transverse offset /mm		
		0	20	40
axial offset /mm	0	1.71	3.17	3.71
	25	2.31	3.47	4.36
	50	2.30	3.31	3.90

Tangential line profile for point source without offset

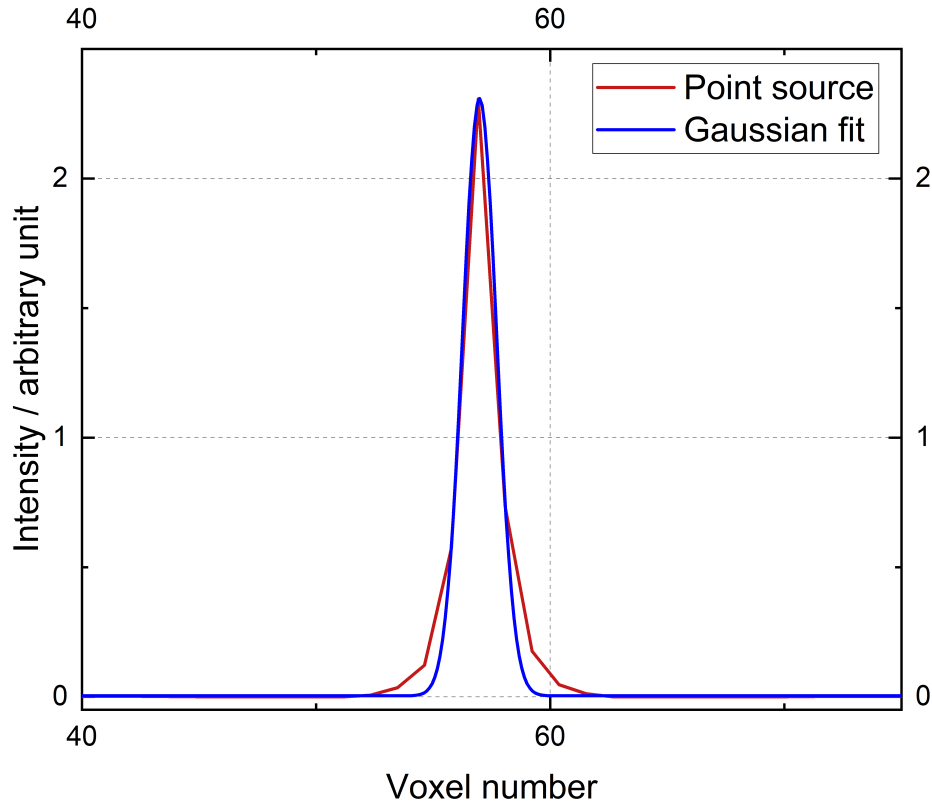


Figure 3.11: Transversal line profile for point source without transverse and axial offset and its Gaussian fit.

The analysis of the results is very promising. Figure 3.11 shows an exemplary measurement with its Gaussian fit both being in a very good agreement. This is an improvement because the edges of the intensity spectrum are much more delimited than in the previous back projections which describes the reality more accurate. The point source in the very middle of the detector has now an FWHM-value which is more than three times lower than the according FWHM-value obtained by the reconstruction using a back projection in section 3.2. Finally, one note that the noise is substantially reduced. Therefore this result is satisfactory.

Table 3.7: Activity ratio and normalization coefficients for different positions in the FOV.

axial offset/mm	transverse offset/mm	Activity ratio	Norm _s	Norm _w
50	0	0.139	1	1
	20	0.184	0.260	0.350
	40	0.178	0.111	0.142
25	0	0.170	1	1
	20	0.172	0.301	0.304
	40	0.186	0.125	0.137
0	0	0.139	1	1
	20	0.172	0.654	0.81
	40	0.163	0.319	0.375

$$\text{experimental activity ratio:} \quad r_{exp} = 0.167 \quad (3.14)$$

$$\text{theoretical activity ratio:} \quad r_{th} = 0.167 \quad (3.15)$$

$$\text{standard deviation:} \quad \sigma_{exp} = 0.017 \quad (3.16)$$

$$\text{relative statistical error:} \quad \frac{\sigma_{exp}}{r_{exp}} = 10 \% \quad (3.17)$$

The results (3.14) to (3.17) unambiguously show that the known activity source interrelations are reconstructed within the statical error boundaries which validates this reconstruction in spite of the fact that in transverse direction the normalization coefficients drop far below one, as it is presented in table 3.7. One notes however, that the deviations in normalization coefficients are expected in the OSMAPOSL reconstruction procedure due to, for example a systematical error with Compton scattering in our normalization measurement.

4 Summary

In this thesis the reconstruction process from the existing ClearPET device was improved, tested and characterized by carrying out a required set of measurements. In what follows, the main results and findings are summarized.

Improvement of the reconstruction process by means of a normalization measurement

In order to monitor improvements in the reconstruction process first of all the state of the initial system was documented in section 3.3 before any changes on the reconstruction process were done. Afterwards the normalization measurement was carried out and the OSMAPOSL algorithm could be applied. It was shown that the OSMAPOSL algorithm improves its behavior in the reconstruction process when the attenuation factor coefficients are considered and multiple iteration are implemented.

In section 3.7 the final results are presented. The FWHM of the reconstruction image was reduced by a factor of three and the blur which occurs when simply back projecting substantially diminished. The interrelations between known source activities have been reconstructed. Some inconsistent behavior of the activities has been observed when their transverse offset changed. There are explanations for this behavior involving Compton scattering, the impact of the OSMAPOSL parameters and the geometry of the cassettes.

Preparation for lab courses This thesis is a good starting point for the lab courses. The homogeneous Sodium-22 phantom makes the handling of the radioactive source possible for the students. Furthermore the measuring time for one single measurement does not exceed four minutes, therefore every aspect of this thesis is reproducible in the lab courses. In addition the theoretical background provides an explanation of the Radon transform so the idea of forward and back projection can be conveyed. To support this, sinograms were extracted from the ClearPET. This thesis in addition to the work of Lehr is the foundation for preparing the task for students and the manual for supervisors.

Outlook There are two main aspects to improve the measurements. First of all the influence of the Compton scattering effect should be eliminated, either by decreasing the energy window in the normalization measurement or by simulating the Compton scattering with STIR utilities.

Especially lowering the energy window is promising because it is simple as it only requires changes of parameters. Both approaches were tried in this thesis but none of them succeeded. The aim is to produce a lab course with the ClearPET for the winter semester 21/22. After doing so it will be possible to further optimize different parameters by slightly changing them between the lab courses. In this way the students can contribute to the improvement of the ClearPET with their measurements.

Bibliography

- [1] D. Le Bars. “Fluorine-18 and medical imaging: Radiopharmaceuticals for positron emission tomography”. In: *Journal of Fluorine Chemistry* 127.11 (2006). The Centenary of Henri Moissan’s Nobel Prize, pp. 1488–1493. ISSN: 0022-1139. DOI: <https://doi.org/10.1016/j.jfluchem.2006.09.015>. URL: <https://www.sciencedirect.com/science/article/pii/S0022113906003083>.
- [2] IAEA - Nuclear Data Section. “Live Chart of Nuclides - nuclear structure and decay data”. <https://www-nds.iaea.org/relnsd/vcharthtml/VChartHTML.html>. June 2021.
- [3] J. Kulenkampff. Private conversation, 2021.
- [4] S. Lehr. “Positronen-Emissions-Tomographie unter Einbeziehung der Pulsform für das physikalische Praktikum”. Bachelor Thesis. Apr. 2020.
- [5] I. Mohammadi et al. “Minimization of parallax error in positron emission tomography using depth of interaction capable detectors: methods and apparatus”. In: *Biomedical Physics & Engineering Express* 5.6 (Oct. 2019), p. 062001. DOI: 10.1088/2057-1976/ab4a1b. URL: <https://doi.org/10.1088/2057-1976/ab4a1b>.
- [6] W. Demtröder. “Experimentalphysik 3 Atome Moleküle und Festkörper”. Springer-Verlag GmbH Deutschland, 2016. DOI: <https://doi-org.wwwdb.dbod.de/10.1007/978-3-662-49094-5>.
- [7] W. Demtröder. “Experimentalphysik 4 Kern-, Teilchen- und Astrophysik”. Springer-Verlag GmbH Deutschland, 2017. DOI: <https://doi-org.wwwdb.dbod.de/10.1007/978-3-662-52884-6>.
- [8] G. F. Knoll. “Radiation detection and measurement”. 2010.
- [9] S. M. Selzer. “ICRU report 85: fundamental quantities and units for ionizing radiation”. In: *Journal of the ICRU* 11.1 (May 2011). URL: <https://eclass.uoa.gr/modules/document/file.php/PHYS215/%CE%92%CE%99%CE%92%CE%9B%CE%99%CE%9F%CE%93%CE%A1%CE%91%CE%A6%CE%99%CE%9A%CE%91%20CE%A3%CE%A5%CE%9C%CE%A0%CE%9B%CE%97%CE%A1%CE%A9%CE%9C%CE%91%CE%A4%CE%91/Thomas%20-%202012%20-%20ICRU%20report%2085%20fundamental%20quantities%20and%20units%20for%20ionizing%20radiation.pdf>.


- [10] K. Thielemans et al. “Software for Tomographic Image Reconstruction”. In: (2021). URL: <http://stir.sourceforge.net/documentation/STIR-UsersGuide.pdf>.
- [11] E. Candes. “Applied Fourier Analysis and Elements of Modern Signal Processing, Lecture 9”. In: (2021).
- [12] E. Candes. “Applied Fourier Analysis and Elements of Modern Signal Processing, Lecture 10”. In: (2021).
- [13] M. Jacobson et al. “Enhanced 3D PET OSEM reconstruction using inter-update Metz filtering”. In: *Physics in Medicine and Biology* 45.8 (July 2000), pp. 2417–2439. DOI: 10.1088/0031-9155/45/8/325. URL: <https://doi.org/10.1088/0031-9155/45/8/325>.
- [14] V. Bettinardi et al. “Implementation and evaluation of a 3D one-step late reconstruction algorithm for 3D positron emission tomography brain studies using median root prior”. In: *European journal of nuclear medicine and molecular imaging* 29 (Feb. 2002), pp. 7–18. DOI: 10.1007/s002590100651.
- [15] M. Defrise et al. “Exact and approximate rebinning algorithms for 3-D PET data”. In: *IEEE Transactions on Medical Imaging* 16.2 (1997), pp. 145–158. DOI: 10.1109/42.563660.

Acknowledgements

At this point I want to thank everybody who supported me during the thesis. A special thanks goes to Dr. Thomas Kormoll. He helped me in every step of my work by answering questions, discussing results and proofreading. In first place, he also was the one who gave me the opportunity to write this thesis. Furthermore I want to emphasize the contribution of Dr. Johannes Kulenkampff for introducing me into his ClearPET workflow and also providing the source code for compiling the manufacturers “rebinning” and “coincidence sorting” functions. Moreover Prof. Krause Rehberg is to be highlighted for providing the Sodium-22 for the phantom. I also want to thank my parents who made it possible to study physics, especially my father, Dr. Markas Sudzius who proofread this thesis too. Furthermore Tim Pokart is to be highlighted. He gave me consultation as friend when measurements did not lead to suitable results and helped me with linguistic design of my work. At the End I want to thank the group members Theresa Werner, Elena Metzner, Vincent Melzer, Marko Gerber who received me in the kindest possible way and especially Dieter Dirk Döhler who prepared a measurement with me.

Erklärung

Hiermit erkläre ich, dass ich diese Arbeit im Rahmen der Betreuung am Institut für Kern und Teilchen Physik ohne unzulässige Hilfe Dritter verfasst und alle Quellen als solche gekennzeichnet habe.

A handwritten signature in black ink, appearing to read 'B. Sudzius'. The signature is fluid and cursive, with a long horizontal stroke at the bottom.

Benas Sudzius

Dresden, Juni 2021

Appendix: Source code

Here the source code for the reconstruction process can be observed. First of all there is the *clearpet.py* file which is analogous to a configuration file.

```
"""
The purpose of this program is to reconstruct .hv files
from the ClearPET. This part of the program stores the variables
required for the reconstruction, whereas function.py performs
the actual reconstruction.

The reconstruction can be invoked from the command line and has following
syntax:

usage: clearpet[-h] [--type [TYPE]] [-a]
arguments:
    -h, --help            show this help message and exit
    --type [TYPE]         --type = OSMAPOSL for reconstruction via OSMAPOSL
                           --type = Back_proj for simple backprojection
                           --type = Clear for managing folders
                           --type = All OSMAPOSL, Back_proj and Clear

Requirements are
    - version 4 of the STIR library or above
    - the normalization .hv file (even for back projection,
      it provides a template for formatting issues)
    - rebinner2_ClearPET and sorter2 command line utility for
      processing of the ClearPETs raw data
    - OSMAPOSL configuration file for OSMAPOSL reconstruction
      and their requirements
    - script made executable as clearpet
"""

import functions as func
import os

def add_directories(parameters):
```

```

"""This function adds parameters to the dictionary"""

parameters['filesdir'] = os.path.join(parameters['pdir'],
                                       'Files_point_source')
parameters['recdir'] = os.path.join(parameters['pdir'],
                                       'Files_point_source')
parameters['normdir'] = os.path.join(parameters['pdir'], 'Norms')
parameters['bin_list'] = [ parameters['prefix'] + '_Prepro1.bin',
                           parameters['prefix'] + '_Prepro2.bin']
parameters['sname'] = parameters['prefix'] + "_sinogramm"
parameters['angName'] = parameters['prefix'] + "_enc.txt"
parameters['outName'] = parameters['prefix'] + "_Coincidences"

return parameters

def main():
    """Main program. Beginning with dictionary which stores
    almost every information."""

    parameters= {
        ##### Parameters for sorter2 #####
        # Name of angular encoder file
        'angName': 'encTime.txt',
        # Name of output file
        'outName': 'Coincidences',
        # Coincidence window in ns
        'coincWin': '12ns',
        # Number of cassettes
        'numCass': '8',
        # Field of view, by number of opposite cassettes
        'FOV': '7',
        # Number of first frame to be processed, 1=first
        'rfrom': '1',
        # Number of last reset frame to be processed 0=all
        'rto': '4',
        # Minimum energy of valid events in keV
        'emin': '250keV',
        # Maximum energy of valid events in keV
        'emax': '750keV',
        # Delay time [ns] for delayed coincidence generation - default = 0
        'delay': None,
    }

```

Appendix

```
# Inner ring radius, in mm
'radius':'135mm',
# Angular offset in degrees
'offset':'17',

##### Further parameters #####
# Current time
'time':None,
# Working parent directory
'pdir':'/home/benas/shared_folder/Reconstruction',
# Sinogram name
'sname':'sinogramm',
# Sinogram tangential dimension in range [50,500]
'tangdim':'99',
# Name of normalization file
'norm_name': 'norm_cyl_750.hv',
# Prefix filename
'prefix': '325_4min_0_Source_400',
# OSMAPOS� configuration file name
'osmaposl_Con':'OSMAPOS�_conf.par',
# List of names of binary files from
'bin_list':[],
# List of file Endings of images
'img_end': ['.v', '.hv'],
# Statfile name
'stat_name':'stat.txt',
# OSMAPOS� suffix for statistics
'osmaposl_suf':'_1'
}

# Update parameters
parameters = add_directories(parameters)

# Start actual reconstruction
func.reconstruct(parameters)

if __name__ == '__main__':
    main()
```

The reconstruction is performed with the *function.py* file.

```
"""This file contains all functions to reconstruct the the activity images
```

```

from the raw data from the ClearPET. They are invoked by clearpet.py"""

import argparse
import os
import subprocess
import time as t
from shutil import copyfile
import textwrap

def timestring():
    """Provides a string with the current time. Necessary for folder names"""

    struct_time = t.gmtime()
    string = ( str(struct_time[3]) + "_"
              + str(struct_time[4]) + "_"
              + str(struct_time[5]) + "___"
              + str(struct_time[2]) + "_"
              + str(struct_time[1]) + "_"
              + str(struct_time[0]))
    return string

def osmaposl(parameters):
    """Runs the OSMAPOSL algorithm utilizing the STIR library"""

    # Changing to working directory
    os.chdir(parameters['workdir'])

    # Running the OSMAPOSL algorithm
    osmaposl_process = subprocess.Popen(["OSMAPOSL",
                                         parameters['osmaposl_Con']],
                                         stdout=subprocess.PIPE)

    output, error = osmaposl_process.communicate()
    print(output)

def back_project(parameters):
    """Runs backprojection using a template image for format purposes"""

    # Changing to working directory
    os.chdir(parameters['workdir'])

    # Running the command via bash

```

```

back_project_process = subprocess.Popen(["back_project",
    parameters['prefix'],
    parameters['sname']+".hs",
    parameters['norm_name']])

output, error = back_project_process.communicate()
print(output)

def rebinner(parameters):
    """Calls the rebinner provided by raytest"""

    Cmd = ["rebinner2_ClearPET",    "-f="+ parameters['FOV'],
        "-o="+ parameters['sname'],
        "-t="+ parameters['tangdim'],
        parameters['outname']]

    process = subprocess.Popen(Cmd, stdout=subprocess.PIPE)
    output, error = process.communicate()
    print(output)

def coincsort(parameters):
    """Calls the coincidence sorter provided by raytest"""

    print('Coincidence sorting...')

    Cmd = ["sorter2",    "-out="+ parameters['outname'],
        "-c="+ parameters['coincWin'],
        "-n="+ parameters['numCass'],
        "-f="+ parameters['FOV'],
        "-emin="+ parameters['emin'],
        "-a="+ parameters['angName'],
        "-emax="+ parameters['emax'],
        "-A="+ parameters['offset'],
        "-rfrom="+ parameters['rfrom'],
        "-rto="+ parameters['rto'],
        parameters['bin_list'][0],
        parameters['bin_list'][1]]

    process = subprocess.Popen(Cmd, stdout=subprocess.PIPE)
    output, error = process.communicate()
    print(output)

```

```

def update_prefixlist(parameters):
    """Gets filenames in orderd in list regarding their types"""

    parameters['prefix_list'] = []
    for file in parameters['worklist']:
        if file[-11:] == "Prepro1.bin":
            parameters['prefix_list'].append(file[:-11])
    return parameters

def update_lines(parameters):
    """Updates parameters of the OSMAPOS1 configuration file"""

    with open(parameters['osmaposl_Con']) as reader:
        lines = reader.readlines()
    with open(parameters['osmaposl_Con'], 'w') as reader:
        for line in lines:
            if line.find('sensitivity filename') != -1:
                line = 'sensitivity filename :=' + \
                    parameters['norm_name'] + '\n'
            if line.find('input file') != -1:
                line = 'input file :=' + parameters['sname'] \
                    + '.hs' + '\n'
            if line.find('initial estimate') != -1:
                line = 'initial estimate :=' + \
                    parameters['norm_name'] + '\n'
            if line.find('output filename prefix') != -1:
                line = 'output filename prefix:= ' + 'OSMAPOS1_' + \
                    parameters['prefix'] + '\n'
            reader.write(line)

def recon_os(parameters, args):
    """Reconstructs the .hv file using bcktest. The reconstructed file
    should only be used as a normalization measurement"""

    # Changes directory
    os.chdir(parameters['workdir'])

    # Gets filenames in orderd in list in regard of their types
    parameters = update_prefixlist(parameters)

```



```

for prefix in parameters['prefix_list']:
    parameters['sname'] = prefix + "sinogramm"
    parameters['outname'] = prefix + "Coincidences"
    parameters['bin_list'] = [ prefix + 'Prepro1.bin',
                              prefix + 'Prepro2.bin']
    parameters['angName'] = prefix + "enc.txt"
    parameters['prefix'] = prefix

    coincsort(parameters)
    rebinner(parameters)
    update_lines(parameters)
    osmaposl(parameters)

def recon_bp(parameters, args):
    """Reconstructs the .hv file using the OSMAPOS algorithm"""

    # Change directory
    os.chdir(parameters['workdir'])

    # Get filenames in orderd in list in regard of their types
    parameters = update_prefixlist(parameters)

    # Set parameters right for each prefix reconstruction
    for prefix in parameters['prefix_list']:
        parameters['sname'] = prefix + "sinogramm"
        parameters['outname'] = prefix + "Coincidences"
        parameters['bin_list'] = [ prefix + 'Prepro1.bin',
                                    prefix + 'Prepro2.bin']
        parameters['angName'] = prefix + "enc.txt"
        parameters['prefix'] = prefix

        coincsort(parameters)
        rebinner(parameters)
        back_project(parameters)

def list_image_info_to_file(parameters, filename):
    """Writes the maximum value for each .hv file. Result is stored
    in a txt file"""

    process_bck = subprocess.Popen(['list_image_info ' + filename +
                                     '| grep max'], shell=True,

```

```

                                stdout=subprocess.PIPE)
output_bck, error_bck = process_bck.communicate()
with open(parameters['stat_name'], "a") as writer:
    output_bck = output_bck.decode('utf8')
    writer.write(filename + ' ' + output_bck)

def stat(parameters, args):
    """Prints the number of total events in the reconstructed file"""

    os.chdir(parameters['workdir'])

    # Ensures that .hv files are detected
    update_prefixlist(parameters)

    if os.path.exists(parameters['stat_name']):
        os.remove(parameters['stat_name'])

    os.mknod(parameters['stat_name'])

    for file in parameters['prefix_list']:
        file_bck = file + '.hv'
        file_osmaposl = 'OSMAPOSL_' + file + parameters['osmaposl_suf'] + '.hv'
        list_image_info_to_file(parameters, file_bck)
        list_image_info_to_file(parameters, file_osmaposl)

def extract_images(parameters, args):
    """Moves all .hv files into a folder"""

    # Ensures that all .hv and .v files are detected
    parameters = update_prefixlist(parameters)

    time = timestring()
    dirname = 'results_' + time

    os.mkdir(dirname)

    for file in parameters['prefix_list']:
        file_bck = [file + '.hv', file + '.v']
        file_osmaposl = ['OSMAPOSL_' + file + parameters['osmaposl_suf'] + '.hv',
                        'OSMAPOSL_' + file + parameters['osmaposl_suf'] + '.v']

```

```

    for filelist in [file_bck, file_osmaposl]:
        for filename in filelist:
            copyfile(filename, os.path.join(dirname, filename))

if os.path.exists(parameters['stat_name']):
    copyfile(parameters['stat_name'],
              os.path.join(dirname, parameters['stat_name']))

def do_all(parameters, args):
    """Performs the whole reconstruction with OSMAPOS,
    Backproj, Stat, Clear """

    recon_bp(parameters, args)
    recon_os(parameters, args)
    stat(parameters, args)
    extract_images(parameters, args)

def parser_handling():
    """This function handles the input from the command line"""

    parser = argparse.ArgumentParser(prog='PROG', conflict_handler='resolve',
                                     description='Reconstruction algorithm for ClearPET',
                                     formatter_class=argparse.RawTextHelpFormatter)

    parser.add_argument(
        '--type', nargs='?',
        help=textwrap.dedent("""\
            --type = OSMAPOS for reconstruction via OSMAPOS
            --type = Back_proj for simple backprojection
            --type = Clear for managing folders\
            --type = All for OSMAPOS, Back_proj, Clear
            """))

    parser.add_argument(
        '--workdir', nargs='?',
        help=textwrap.dedent("""\
            --workdir = path to the directory with Files
            """))

    )

    parser.add_argument(

```

```

        '-a', '--all', action='store_true',
        help=textwrap.dedent("""\
            applies requiered operation to all available files""")
    )

    parser.add_argument('-s', "--savetime", action='store_true',
        help=textwrap.dedent("""\
            saves time. Does not copy binary files to
            destination, neither it does Coincidence sorting
            nor Rebinning"""))

    args = vars(parser.parse_args())
    return args

def reconstruct(parameters):
    """This function is called by clearpet.py and coordinates the programm"""
    # Handling parsers for optimized command line input
    args = parser_handling()

    # Set the workdir as directory, from which programm is called in bash
    parameters['workdir'] = os.getcwd()

    # Get a list of all files in workdir
    parameters['worklist'] = []
    for (dirpath, dirname, filenames) in os.walk(parameters['workdir']):
        parameters['worklist'].extend(filenames)
        break

    # Decide if reconstrucion or different task
    if args.get('type')=='OSMAPOSL':
        recon_os(parameters, args)
    elif args.get('type')=='Back_proj':
        recon_bp(parameters, args)
    elif args.get('type')=='Stat':
        stat(parameters, args)
    elif args.get('type')=='Clear':
        extract_images(parameters, args)
    elif args.get('type')=='All':
        do_all(parameters, args)
    else:

```

```
raise ValueError('No measurement type specified')
```